Ocean Engineering 303 (2024) 117760

Contents lists available at ScienceDirect

Ocean Engineering

journal homepage: www.elsevier.com/locate/oceaneng

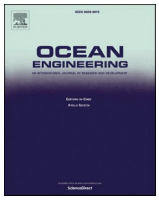

Research paper

Analysis of railway vehicle-track interaction performance in submerged floating tunnel subjected to wave excitations

Yang Song [a,b,c], Jian Dai [c,*], Albert Lau [d]

[a] National Rail Transit Electrification and Automation Engineering Technique Research Centre, Southwest Jiaotong University, 610031, Chengdu, China
[b] SWJTU-Leeds Joint School, Southwest Jiaotong University, 610031, Chengdu, China
[c] Department of Built Environment, Oslo Metropolitan University, 0166, Oslo, Norway
[d] Department of Civil and Environmental Engineering, Norwegian University of Science and Technology, 7491, Trondheim, Norway

ARTICLE INFO

Keywords:
Railway
Submerged floating tunnel
Vehicle-track interaction
Stochastic analysis
Wave excitations

ABSTRACT

Submerged Floating Tunnels (SFTs) are an innovative and appealing solution for the water crossing of railways over wide and deep waterbodies where it is challenging or even impractical to construct conventional bottom-founded bridges or immersed tunnels. This study aims to develop a dynamic model for examining the behaviours of the coupled train-track-SFT system under various wave conditions and track irregularities. In this study, the SFT tube is idealised as an Euler-Bernoulli beam with flexible supports and combined with a train-ballasted track model to develop the vertical coupling dynamics model of the train-track-SFT system. Random wave excitations are generated using the JONSWAP spectra, and the Monte Carlo analysis is employed to evaluate the dynamic responses of both the SFT and the train carbody, considering the stochastic nature of the waves and the track irregularities. The effects of different longitudinal spacings between mooring lines, train speeds, wave headings, and wave characteristics on the dynamic responses of the coupled system are investigated. The analysis results indicate that train travel within the SFT under operational wave conditions is generally safe. However, significant instability may occur when the longitudinal spacing between mooring lines is large enough and the system's natural frequency is close to the frequencies of the waves, leading to an increased possibility of resonance. Moreover, longer wave peak periods, higher significant wave heights and lower SFT installation depths are found to exacerbate the degree of vibration of both the SFT and carbody, which may lead to higher dispersion of dynamic behaviours.

1. Introduction

The development of submerged floating tunnels (SFTs) stems from the need to overcome transportation challenges posed by large bodies of water while minimising environmental impact and maximising connectivity. Compared with previous infrastructure options such as floating bridges, immersed tunnels, and bottom founded structures, SFTs provide greater flexibility in terms of alignment and route selection, more efficient and less time-consuming construction process, as well as lower environmental impact. The concept of SFT has gained attraction as an innovative alternative to traditional bridge or tunnel construction methods (Zhang et al., 2021).

Railways are known for their high transport capacity, efficiency and speed. They are particularly effective for moving large volumes of people or goods over long distances (Liu et al., 2023; Zhang et al., 2013). Incorporating railways into submerged floating tunnels would provide an innovative solution for sea-crossing railways over straits or deep fjords where it is challenging or even impractical to construct conventional bottom-founded bridges or immersed tunnels. As shown in Fig. 1, this type of tunnel is designed to be submerged below the water surface, held in place by station-keeping systems, and provides a stable pathway for trains to travel across the water.

1.1. Problem descriptions

Different from the land railway system, the railway system in SFT is subjected to some unique challenges posed by harsh and random wave excitations (Jiang et al., 2018). The wave excitations can trigger the vibration of SFT, which directly affects the operation of the train. Some previous studies have indicated that the vertical vibration of the SFT

* Corresponding author.
E-mail address: jiandai@oslomet.no (J. Dai).

https://doi.org/10.1016/j.oceaneng.2024.117760
Received 17 October 2023; Received in revised form 13 February 2024; Accepted 2 April 2024
Available online 9 April 2024

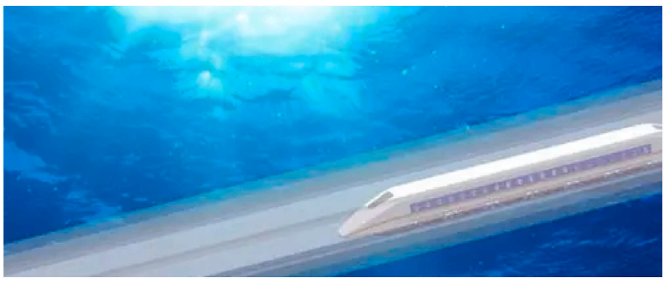

Fig. 1. Conceptual picture of high-speed train in an SFT.

under wave excitations is more considerable than the motions in other directions, which is most relevant to safety and comfortability (Luo et al., 2021). In particular, the wave excitation may trigger the resonance of the SFT under some specific environmental conditions, which should be revealed in preliminary feasibility research to avoid fatal accidents. Therefore, the coupling dynamic performance of the train-track-SFT system should be comprehensively and accurately evaluated to ensure the safe design of such a critical transport infrastructure.

1.2. Literature review

The preliminary concept of SFTs can be traced back to the first decades of the 20th century (Kunisu et al., 1994). Several feasibility studies and schemes have been performed for various straits and lakes, such as China's Qiandao Lake (Martinelli et al., 2011), Italy's Strait of Messina (Martire et al., 2010), Norway's Hogsfjord Strait (Moan and Eidem, 2020), and Japan's Funka Bay (Kanie, 2010). Unlike traditional transportation structures, SFTs works under the excitations of waves and currents in the marine environment (Xiang and Yang, 2016). The Morison equation is commonly employed to obtaining the fluid force-acting on SFT owing to its slenderness. The equation proposed by Morison assumes that the wave forces acting on SFTs can be seen as the summation of the inertial force and the drag force components, which are determined by the relative velocity and acceleration of SFTs with respect to the wave particles. The significant applications of the Morison equation to SFTs can be found in (Seo et al., 2015). Another method to determine the wave forces is the diffraction theory proposed by MacCamy and Fuchs, 1954 (RC MacCamy and RA Fuchs, 1954). Based on this assumption, the velocity potential is divided into the incident potential, radiation potential and diffraction potential. The applications of the diffraction theory can be seen in (Chakrabarti et al., 2007; Paik et al., 2004). The comparative analysis in (Kunisu, 2010) indicates that both approaches can yield accurate hydrodynamic calculations in normal construction conditions. The fluid-structure interaction analysis of a SFT was initiated in (Remseth et al., 1999). The random dynamic responses of a SFT caused by wave excitations were evaluated via a stochastic analysis. In (Martinelli et al., 2010), the response spectrum of a SFT was evaluated using a median pseudo-acceleration response spectrum method.

Apart from the wave excitations, SFTs are also subjected to the moving load as a transportation infrastructure. The research on the moving vehicle effects on a structure has attracted a number of scholars due to its application potential in various industrial backgrounds (Ouyang, 2011). With the development of the numerical simulation technique, various types of models are advanced to study the coupling dynamics of vehicle-structure interaction, including the vehicle-bridge models (Chen et al., 2021), the high-speed train-track coupling models (Wang et al., 2019; Zhai et al., 2019), as well as the pantograph-overhead contact line interaction models (Song et al., 2020, 2021, 2023b). As for the SFT subjected to a moving load, several scholars have analysed the interaction performance of vehicle-SFT based on numerical analysis or explicit solutions (Yang et al., 2022a). In (Tariverdilo et al., 2011), the equation of motion for a SFT traversed by a moving load was developed based on the elastic beam theory on elastic foundations. The influence of anchoring properties on the SFT's behaviours excited by a moving load was further investigated in (Zhang and Yang, 2016). Instead of using a moving force, the inertia effect of the vehicle model was considered in (Yang et al., 2022b) to analyse the interaction behaviours of a coupled vehicle-SFT system and determine the dominant factors affecting the SFT's dynamic response. The acceptance of the numerical model of the coupled vehicle-SFT system was validated by experiment tests in (Xiang et al., 2021). Concerning a railway SFT, the trains are usually represented as rigid multi-body systems. The structure safety of SFT and the passenger comfort were evaluated considering the environmental wave excitations in (Jin et al., 2021; Jin and Kim, 2020). In (Gao et al., 2022), a new analytical model for analysing a SFT with moving loads was proposed based on the mode superposition method, and the analytical solution was validated via an finite element model. Based on the Lagrange equation, an analytical model considering the vehicle and tethers was developed in (Luo et al., 2021), which can consider more complicated boundary conditions. Considering the eccentric load effect of vehicles in a SFT, the vehicle-SFT coupling vibration equations under the action of a motorcade running on one lane of the roadway were developed (Yang et al., 2021), and the solutions were validated through comparison with the finite element method.

The above literature review reveals that the accuracy of the finite element model of the SFT has been widely acknowledged and accepted as the standard for validating other emerging analytical models. According to the research presented in (Lin et al., 2018), the vertical movement resulting from the interaction between the vehicle and the SFT is identified as the primary factor influencing passenger comfort. On the other hand, the transverse motion is primarily induced by currents rather than waves. The former is typically considered a quasi-static load, leading to SFT deviation rather than short-time period fluctuation (Wu et al., 2021). Consequently, the vertical motion caused by wave excitations has a more significant impact on the performance of the vehicle-SFT interaction.

1.3. scope and contribution of this work

Upon reviewing the existing literature, it becomes evident that further investigation into the performance of railway vehicle-SFT interaction is warranted due to several gaps in current research. These gaps include:

1) In previous studies, the track system's substructures have been largely overlooked, resulting in an incomplete representation of the dynamic behaviours of the train-track-SFT interaction.
2) The quantification of stochastics in dynamic responses, caused by wave excitations and track irregularities, has been lacking in previous research. Such quantification is crucial for safety and comfort assessments.
3) The influence of SFT configuration (specifically mooring length) and working conditions (such as speed and installation depth of SFT) on the vehicle-track interaction remains inadequately understood. Understanding these effects is vital for designing SFTs for railway services.

To address these aforementioned issues, this paper presents a comprehensive analysis of the stochastic responses exhibited by a coupled train-track-SFT system. Utilizing a finite element model of the track-SFT system, the study focuses on simulating the vertical interaction between the train, track, and SFT. The numerical model incorporates random excitations from waves and track irregularities, and the Monte Carlo method is employed to obtain stochastic dynamic responses. The numerical simulations consider two wave conditions, specifically the design operational and design storm conditions, aiming

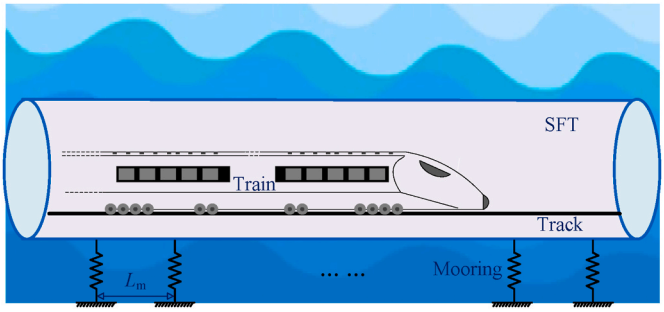

Fig. 2. SFT model with moorings.

to investigate the influence of crucial SFT parameters, train speed, wave headings and SFT installation depths on the dynamic behaviours of the carbody and SFT. This academic study aims to comprehensively analyse the impact of key structural parameters on the performance of vehicle-track interaction. Unlike a case study focused on specific real-world objects, this research seeks to elucidate the broader implications of various structural factors on the overall dynamic behaviour and functionality of the vehicle-track system.

1.4. The organisation of this paper

The present section has provided an overview of the background and literature review. The remainder of this paper is structured as follows: Section 2 presents a comprehensive explanation of the vehicle-track-SFT system model, incorporating wave excitations. The intricate dynamics of the system are captured and analysed. In Section 3, the interaction performance of the system under operational wave conditions is thoroughly examined. Various factors, such as wave headings and train speed, are taken into account to assess their influence on the system's behaviour. Section 4 focuses on investigating the system's response under extreme wave conditions. This analysis considers critical scenarios to evaluate the system's robustness and safety. Finally, in Section 5, the main conclusions drawn from the study are discussed, highlighting key findings and implications. Additionally, potential avenues for future research and improvements in the field are also addressed.

2. Modelling of vehicle-track-SFT system

Fig. 2 depicts the vehicle-track-SFT model, which encompasses the integration of a SFT model within the conventional vehicle-track model. This holistic coupling model is established by incorporating the conventional vehicle-track model inside a SFT model. Specifically, the SFT experiences intricate wave excitations that directly impact railway operations. This section provides a comprehensive description of the SFT model and the wave excitations, followed by an explanation of how the vehicle-track-SFT coupling model is implemented.

2.1. SFT model and wave excitations

The SFT is modelled as Euler-Bernoulli beam elements supported by several mooring lines to limit its horizontal and vertical motions. The effect of moorings can be reasonably treated as springs with equivalent stiffnesses at a uniform longitudinal interval of L_m. It is important to emphasize that this assumption effectively captures the vertical dynamics of the SFT. However, it is crucial to acknowledge that this simplified representation may require adjustments when delving into the analysis of spatial movement. The equation of motion for the SFT can be represented as follows (Øiseth et al., 2014; Dai et al., 2020)

$$\mathbf{M}_S\ddot{\mathbf{U}}_S + \mathbf{C}_S\dot{\mathbf{U}}_S + \mathbf{K}_S\mathbf{U}_S = \mathbf{F}_S \tag{1}$$

where $\mathbf{M}_S$, $\mathbf{C}_S$ and $\mathbf{K}_S$ are the structural mass, damping and stiffness matrices of the SFT, respectively. $\ddot{\mathbf{U}}_S$, $\dot{\mathbf{U}}_S$ and $\mathbf{U}_S$ are the acceleration, velocity and displacement vectors of the SFT, respectively. $\mathbf{F}_S$ is the external force vector including the wave loads and the vehicle loads. A damping ratio of 0.025 is adopted in the study. The element structural stiffness matrix $\mathbf{K}_S^e$ of the SFT, which can be expressed by

$$\mathbf{K}_S^e = E_sI_s\int_0^{l_{es}}\frac{\partial^2\mathbf{N}_s^T}{\partial x^2}\frac{\partial^2\mathbf{N}_s}{\partial x^2}\mathrm{d}x \tag{2}$$

where E_sI_s is the flexural rigidity of the SFT about its strong axis, l_{es} is the element length of the SFT, and $\mathbf{N}_s$ is the matrix of the Hermitian cubic shape functions of the Euler-Bernoulli beam.

This paper focused on the wave load effects on the vertical motions of an SFT and thus the horizontal motions and their effects are not investigated. According to Morison's equation (Luo et al., 2021; Dai et al., 2022), the wave force per unit length acting on the SFT in the vertical direction can be expressed by.

$$f_W = \frac{1}{4}\pi D^2\rho_w\dot{u}(t) + \frac{1}{4}C_a\pi D^2\rho_w\left(\dot{u}(t) - \frac{\partial^2 w(x,t)}{\partial t^2}\right) + \frac{1}{2}C_d\rho_w D\left|u(t) - \frac{\partial w(x,t)}{\partial t}\right|\left(u(t) - \frac{\partial w(x,t)}{\partial t}\right) \tag{3}$$

in which u is the vertical wave velocity, w is the vertical dynamic deflection of the SFT. C_a and C_d are the added mass and drag coefficients, respectively. D is the diameter of the SFT. ρ_w denotes the density of seawater. Note that the three terms on the right-hand side denote the Froude-Krylov force, the hydrodynamic mass force, and the viscous drag force, respectively. The viscous drag force is quadratic and has to be linearized for the numerical computation. By applying the irregular-wave stochastic linearization approach (Shao et al., 2016), the linearized equivalent viscous drag force per unit length of the SFT is given by

$$f_D = \frac{1}{2}C_d\rho_w D\left|u(t) - \frac{\partial w(x,t)}{\partial t}\right|\left(u(t) - \frac{\partial w(x,t)}{\partial t}\right) = \frac{1}{2}C_d\rho_w D\sqrt{\frac{8}{\pi}}\sigma_{\left|u(t)-\frac{\partial w(x,t)}{\partial t}\right|}\left(u(t) - \frac{\partial w(x,t)}{\partial t}\right) = b\left(u(t) - \frac{\partial w(x,t)}{\partial t}\right) \tag{4}$$

where the term b is the linearized damping coefficient contributed by a strip of the SFT of unit length. $\sigma_{\left|u(t)-\frac{\partial w(x,t)}{\partial t}\right|}$ is the standard deviation of the amplitude of the relative vertical velocity between the flow and the SFT. Note that the linearized damping coefficient b depends on the motion of the SFT and thus the evaluation requires an iterative process. The elementary force vector $\mathbf{F}_W^e$ for each SFT element can thus be expressed by

$$\mathbf{F}_W^e = \int_0^{l_{es}}\mathbf{N}_s^T f_{d1}\mathrm{d}x = \frac{1}{4}\pi(1+C_a)D^2\rho_w\int_0^{l_{es}}\mathbf{N}_s^T\dot{u}(t)\mathrm{d}x - \frac{1}{4}\pi C_aD^2\rho_w\int_0^{l_{es}}\mathbf{N}_s^T\mathbf{N}_s\mathrm{d}x\ddot{\mathbf{U}}_S^e + b\left(\int_0^{l_{es}}\mathbf{N}_s^T u(t)\mathrm{d}x - \int_0^{l_{es}}\mathbf{N}_s^T\mathbf{N}_s\mathrm{d}x\dot{\mathbf{U}}_S^e\right) \tag{5}$$

As the hydrodynamic mass force is a function of the acceleration of the SFT and the viscous drag force is a function of the velocity of the SFT, the governing equation of motion for a SFT element corresponding to Eq. (1) can be rewritten as

$$\left(\mathbf{M}_S^e + \mathbf{M}_A^e\right)\ddot{\mathbf{U}}_S^e + \left(\mathbf{C}_S^e + \mathbf{C}_D^e\right)\dot{\mathbf{U}}_S^e + \mathbf{K}_S^e\mathbf{U}_S^e = \mathbf{F}_{exc}^e + \mathbf{F}_{veh}^e \tag{6}$$

where $\mathbf{M}_A^e$ and $\mathbf{C}_S^e$ denote the element structural mass and damping matrices, respectively. $\mathbf{M}_A^e$ and $\mathbf{C}_D^e$ denote the element added mass and viscous damping matrices due to the fluid, respectively. $\ddot{\mathbf{U}}_S^e$, $\dot{\mathbf{U}}_S^e$ and $\mathbf{U}_S^e$ are the element acceleration, velocity and displacement vectors, respectively. $\mathbf{F}_{exc}^e$ refers to the element wave excitation load vector, and $\mathbf{F}_{veh}^e$ is the element vehicle load vector. The element added mass and

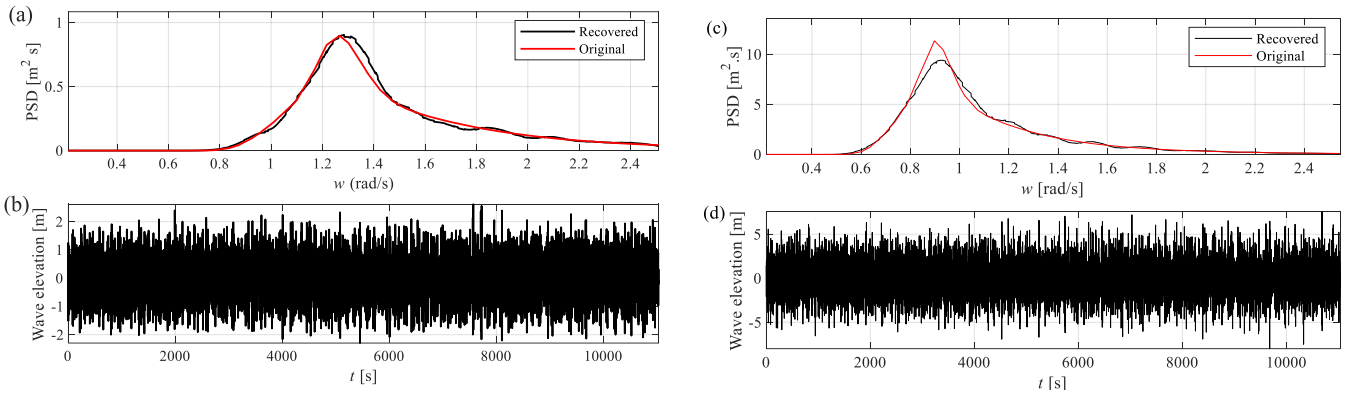

Fig. 3. Wave elevation time history and corresponding PSD: (a) PSD for operational wave condition; (b) time history of wave elevation for operational wave condition; (c) PSD for rough wave condition; (b) time history of wave elevation for rough wave condition.

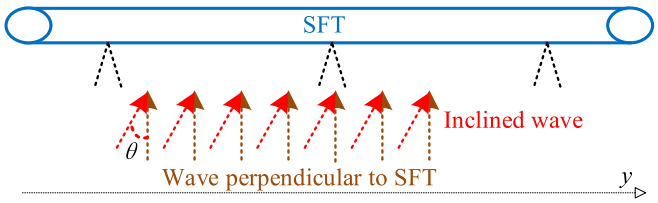

Fig. 4. Schematic of SFT subjected to wave with an inclination angle.

viscous damping matrices as well as the wave excitation load vector are given by

$$\mathbf{M}_{\mathrm{A}}^{\mathrm{e}} = \frac{1}{4}\pi C_{\mathrm{a}} D^2 \rho_w \int_0^{l_{es}} \mathbf{N}_{\mathrm{s}}^{\mathrm{T}} \mathbf{N}_{\mathrm{s}} \mathrm{d}x \tag{7a}$$

$$\mathbf{C}_{\mathrm{D}}^{\mathrm{e}} = b \int_0^{l_{es}} \mathbf{N}_{\mathrm{s}}^{\mathrm{T}} \mathbf{N}_{\mathrm{s}} \mathrm{d}x \tag{7b}$$

$$\mathbf{F}_{\mathrm{exc}}^{\mathrm{e}} = \frac{1}{4}\pi(1+C_{\mathrm{a}}) D^2 \rho_w \int_0^{l_{es}} \mathbf{N}_{\mathrm{s}}^{\mathrm{T}} \dot{u}(t) \mathrm{d}x + b \int_0^{l_{es}} \mathbf{N}_{\mathrm{s}}^{\mathrm{T}} u(t) \mathrm{d}x \tag{7c}$$

The JONSWAP spectrum is used to generate the time history of vertical wave velocity u. The JONSWAP spectrum, also known as the Joint North Sea Wave Project spectrum, is a widely used empirical model for representing the shape of ocean wave energy distribution as a function of frequency. By incorporating field measurements and empirical observations, the JONSWAP spectrum offers a practical tool for characterising ocean wave conditions and assessing their impact on marine systems. Mathematically the JONSWAP spectrum can be expressed as (Guo and Xu, 2011)

$$S(f) = \gamma * \alpha^2 * g^2 \Big/ f^5 * \exp\left(-\beta * \left(f/f_{\mathrm{p}}\right)^4\right) \tag{8}$$

in which $S(f)$ represents the wave energy spectrum density at a given frequency f. γ is the peak enhancement factor and represents the ratio of the measured significant wave height to the significant wave height predicted by the linear wave theory. α is the dimensionless peak enhancement parameter and is related to the steepness of the wave spectrum, which is defined as

$$\alpha = 0.076 * (H_{\mathrm{s}}/g)^{0.22} * \gamma^{0.33} \tag{9}$$

where H_{s} is the significant wave height, and g is the acceleration due to gravity. f is the frequency at which the wave energy is being evaluated. f_{p} is the peak frequency of the wave spectrum, which represents the dominant frequency, which is related to the peak period T_{p} as

$$f_{\mathrm{p}} = 1 \Big/ T_{\mathrm{p}} \tag{10}$$

β is the peak enhancement factor decay parameter and is given by:

$$\beta = 5.0 * f_{\mathrm{m}} \Big/ f_{\mathrm{p}} \tag{11}$$

where f_{m} is the spectral peak frequency at the measurement site. In this paper, the coefficients in the JONSWAP spectrum are selected from (Jin and Kim, 2020). Using the inverse Fourier Transform, the time history of wave elevation can be generated from the spectrum.

Taking a typical operational wave condition, $H_{\mathrm{s}} = 3$ m, $T_{\mathrm{p}} = 5$ s and a rough wave condition, $H_{\mathrm{s}} = 9$ m, $T_{\mathrm{p}} = 7$ s as examples, one case of wave elevation time history and the comparison of PSD is presented in Fig. 3. It is observed from Fig. 3(a) and (b) that the wave elevation spectrum

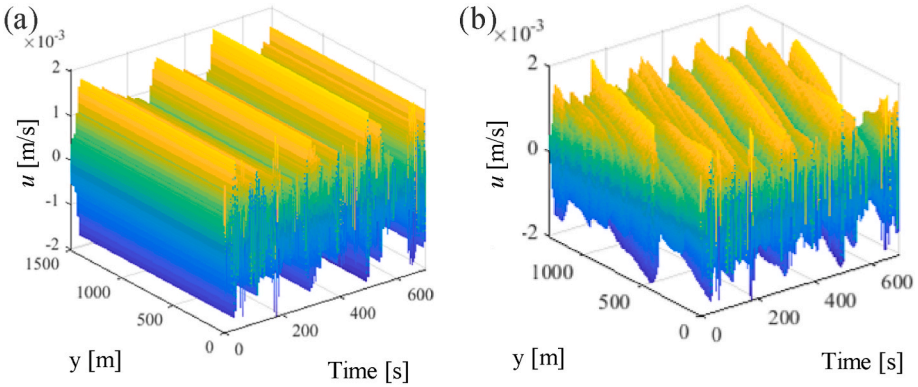

Fig. 5. Wave velocity with different headings. (a) Presents the results with $\theta = 90°$; (b) presents the results with $\theta = 30°$.

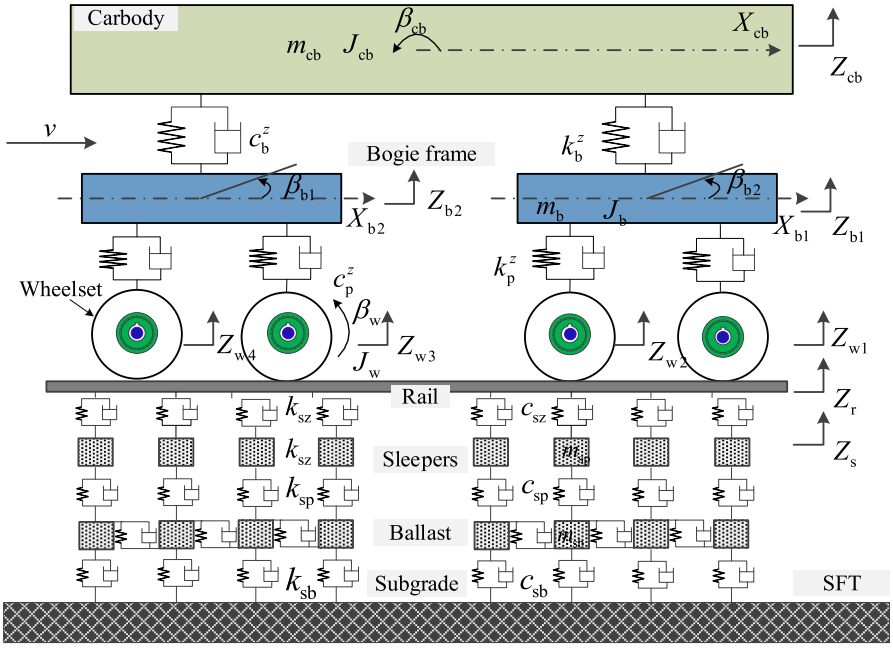

Fig. 6. Vehicle-track-SFT coupled dynamics model.

Table 1
Main parameters of vehicle-track-SFT system used in the case study.

	Parameter	Value
SFT	Young's Modulus	3×10^{10} N/m^2
	Moment of inertia	7.8×10^3
	Total length	1500 m
	Tunnel outer diameter	23 m
	Inclination of the moorings	40°
	Distance from centre to seabed	40 m
	SFT mass per unit length	3.7×10^5 kg/m
	Tether stiffness	1.17×10^8 N/m
Vehicle	Carbody mass	43862.5 kg
	Bogie mass	2400 kg
	Wheelset mass	1850 kg
	Carbody mass moment of inertia	1.65×10^6 kg m^2
	Bogie mass moment of inertia	1.31×10^3 kg m^2
	Wheelset mass moment of inertia	123 kg m^2
	Primary suspension stiffness	1.9×10^5 N/m
	Primary suspension damping	4.0×10^4 N/m
	Secondary suspension stiffness	1.18×10^5 N/m
	Secondary suspension damping	1.3×10^4 N/m
	Semi-distance between bogies	8.75 m
	Semi-distance between wheelsets in bogies	1.25 m
	Wheel radius	0.43 m
Track	Young's modulus	2.06×10^{11} N/m2
	Rail second moment of area	3.217×10^{-5} m^4
	Rail mass per unit length	60.64 kg/m
	Fastener stiffness	6.0×10^7 kg/m
	Fastener damping	5.0×10^4 N/s m
	Sleeper spacing	0.6 m
	Sleeper mass (half)	170 kg
	Ballast mass	340 kg
	Ballast stiffness	1.2×10^8 N/m
	Ballast damping	6×10^4 N/s m
	Subgrade stiffness	1.9×10^8 N/m
	Subgrade damping	1.0×10^5 N/s m

peaks at around 1.26 rad/s, related to $T_p = 5$s. From Fig. 3(c) and (d), the wave elevation spectrum peaks at around 0.9 rad/s, related to $T_p = 7$ s. The recovered and original spectrums show an acceptable consistency, demonstrating the acceptance of the accuracy of generating the wave elevation.

According to the Airy wave theory and intermediate-water assumption, the vertical fluid particle velocity can be estimated by

$$u = \sigma a \frac{\sinh k(z+h)}{\sinh kh} \sin(\omega t + \varphi) \tag{12}$$

where $a = H/2$ represents the wave amplitude, $\omega = 2\pi/T$ is the incident wave angular frequency, and k is the wave number, which satisfies $\omega^2 = gk$ where g denotes the gravitational acceleration. h is the water depth, and z is the SFT position relative to the water surface. For this analysis, the deep water scenario is mostly examined, with a specific value of 60 m assigned to z. Furthermore, the effect of varying SFT submergence depths is also explored in subsequent analyses.

When the wave heading is perpendicular to the SFT, i.e., the beam sea condition, the wave components reach the whole SFT with the same excitation velocity at the same instant. However, if an inclination angle θ between the wave and the SFT is not 90°, i.e., the oblique wave conditions, the vertical wave velocities acting on different positions of the SFT at the same time instant are not expected to be the same. As illustrated in Fig. 4, the spatial positions of the whole SFT on the y-axis are not uniform, resulting in a phase difference in the waves acting on different positions. Therefore, Eq. (12) takes the following form:

$$u(y_{\text{sft}}, t) = a\omega e^{kz} \sin\left(\omega\left(t - \frac{y_{\text{sft}}}{c}\right) + \varphi\right) \tag{13}$$

In the revised equation, c represents the wave speed, while y_{sft} denotes the y-axis coordinate of each position within the SFT, accounting for the variation in wave phase. Fig. 5(a) illustrates the vertical wave velocity acting on the SFT in relation to the spatial position and time under beam sea conditions ($\theta = 90°$). The SFT plays a crucial role in connecting the land parcels separated by water bodies, which represent a region prone to sea waves that typically align with the direction of the strait, leading to an approximately 90° wave heading angle with respect to the span direction of the SFT. This often signifies the most unfavorable design scenario, and in the context of engineering design practice, it deserves primary attention and consideration. It can be observed that the vertical wave velocity acting on the entire SFT remains consistent at each time instant. However, when considering an inclination of the wave heading, the vertical wave velocity demonstrates notable misalignment along the SFT at each time instant, as depicted in Fig. 5(b). The impact of waves

with different headings will be further investigated in the subsequent section.

2.2. Vehicle-track-SFT model

As shown in Fig. 6, the vehicle model is comprised of a carbody, two bogies, four wheelsets and two-stage suspensions. All these components are modelled as multiple rigid bodies interconnected by spring and dashpot units. Based on the multi-body dynamics, the equation of motion for the vehicle can be written in a compact matrix form as

$$\mathbf{M}_{\mathrm{V}}\ddot{\mathbf{U}}_{\mathrm{V}} + \mathbf{C}_{\mathrm{V}}\dot{\mathbf{U}}_{\mathrm{V}} + \mathbf{K}_{\mathrm{V}}\mathbf{U}_{\mathrm{V}} = \mathbf{F}_{\mathrm{V}} \tag{14}$$

where, $\mathbf{M}_{\mathrm{V}}$, $\mathbf{C}_{\mathrm{V}}$ and $\mathbf{K}_{\mathrm{V}}$ are the mass, damping and stiffness matrices of the vehicle, respectively. $\ddot{\mathbf{U}}_{\mathrm{V}}$, $\dot{\mathbf{U}}_{\mathrm{V}}$ and $\mathbf{U}_{\mathrm{V}}$ are the acceleration, velocity and displacement vectors of the vehicle, respectively. $\mathbf{F}_{\mathrm{V}}$ is the external force vector.

The track model consists of the rail and sleepers. The rail is modelled by the Euler-Bernoulli beam theory. The sleeper and ballasts are described as lumped mass elements with equivalent stiffness and damping coefficients. According to the finite element method, the equation of motion for the track system can be written as

$$\mathbf{M}_{\mathrm{T}}\ddot{\mathbf{U}}_{\mathrm{T}} + \mathbf{C}_{\mathrm{T}}\dot{\mathbf{U}}_{\mathrm{T}} + \mathbf{K}_{\mathrm{T}}\mathbf{U}_{\mathrm{T}} = \mathbf{F}_{\mathrm{T}} \tag{15}$$

a similar form with Eq. (2).

The wheel-rail interaction is realised by the nonlinear Hertzian elastic contact theory. The contact force $F_{\mathrm{VT}}(t)$ is calculated by the Hertzian wheel-rail constant coefficient G and the indentation $\delta Z_{\mathrm{VT}}(t)$ of contact surface between wheels and rail as follows (Zhai, 2020):

$$F_{\mathrm{VT}}(t) = \begin{cases} \left[\frac{1}{G}\delta Z_{\mathrm{VT}}(t)\right]^{3/2} & if \ \ \delta Z_{\mathrm{VT}}(t) > 0 \\ 0 \quad if \ \ \delta Z_{\mathrm{VT}}(t) \le 0 \end{cases} \tag{17}$$

The track irregularities are the main source of the vibration of the vehicle. This study adopts the German track irregularity spectrum for high-speed railway. The power spectral density (PSD) function can be written as follows (Zhai, 2020):

$$S_{\mathrm{z}}(\Omega_{\mathrm{m}}) = \frac{A_z\Omega_{\mathrm{c}}^2}{\left(\Omega_{\mathrm{m}}^2 + \Omega_{\mathrm{r}}^2\right)\left(\Omega_{\mathrm{m}}^2 + \Omega_{\mathrm{c}}^2\right)} \tag{18}$$

where S_{z} denotes the PSD function of the track irregularity. Ω_{m} is the frequency. A_z is the roughness coefficient, Ω_{r} and Ω_{c} are the cut-off frequencies. The time history of track irregularities can be obtained by inversing S_{z} through inverse Fast Fourier Transform.

The equation of motion for the whole vehicle-track-SFT system can be assembled as follows:

$$\begin{bmatrix} \mathbf{M}_{\mathrm{V}} & & \\ & \mathbf{M}_{\mathrm{T}} & \\ & & \mathbf{M}_{\mathrm{S}} \end{bmatrix} \begin{bmatrix} \ddot{\mathbf{U}}_{\mathrm{V}} \\ \ddot{\mathbf{U}}_{\mathrm{T}} \\ \ddot{\mathbf{U}}_{\mathrm{S}} \end{bmatrix} + \begin{bmatrix} \mathbf{C}_{\mathrm{V}} & & \\ & \mathbf{C}_{\mathrm{T}} & \mathbf{C}_{\mathrm{TS}} \\ & \mathbf{C}_{\mathrm{ST}} & \mathbf{C}_{\mathrm{S}} \end{bmatrix} \begin{bmatrix} \dot{\mathbf{U}}_{\mathrm{V}} \\ \dot{\mathbf{U}}_{\mathrm{T}} \\ \dot{\mathbf{U}}_{\mathrm{S}} \end{bmatrix} + \begin{bmatrix} \mathbf{K}_{\mathrm{V}} & \mathbf{K}_{\mathrm{VT}} & \\ \mathbf{K}_{\mathrm{TV}} & \mathbf{K}_{\mathrm{T}} & \mathbf{K}_{\mathrm{TS}} \\ & \mathbf{K}_{\mathrm{ST}} & \mathbf{K}_{\mathrm{S}} \end{bmatrix} \begin{bmatrix} \dot{\mathbf{U}}_{\mathrm{V}} \\ \dot{\mathbf{U}}_{\mathrm{T}} \\ \dot{\mathbf{U}}_{\mathrm{S}} \end{bmatrix} = \begin{bmatrix} \mathbf{F}_{\mathrm{V}} \\ \mathbf{F}_{\mathrm{T}} \\ \mathbf{F}_{\mathrm{S}} \end{bmatrix} \tag{19}$$

in which, $\ddot{\mathbf{U}}_{\mathrm{T}}$, $\dot{\mathbf{U}}_{\mathrm{T}}$ and $\mathbf{U}_{\mathrm{T}}$ are the global acceleration, velocity and displacement vectors of the track system, respectively. $\mathbf{F}_{\mathrm{T}}$ is the external force vector including the vehicle loads. The mass matrix $\mathbf{M}_{\mathrm{T}}$, the damping matrix $\mathbf{C}_{\mathrm{T}}$ and the stiffness matrix $\mathbf{K}_{\mathrm{T}}$ can be assembled by the element matrices $\mathbf{M}^{\mathrm{e}}_{\mathrm{t},n}$, $\mathbf{C}^{\mathrm{e}}_{\mathrm{t},n}$ and $\mathbf{K}^{\mathrm{e}}_{\mathrm{t},n}$ of the nth track segment. The element stiffness matrix $\mathbf{K}^{\mathrm{e}}_{\mathrm{t},n}$ can be written as

$$\mathbf{K}^{\mathrm{e}}_{\mathrm{t},n} = \mathbf{K}^{\mathrm{e}}_{\mathrm{r},n} + \mathbf{K}^{\mathrm{e}}_{\mathrm{r-s},n} + \mathbf{K}^{\mathrm{e}}_{\mathrm{s-d},n} \tag{16}$$

in which $\mathbf{K}^{\mathrm{e}}_{\mathrm{r-s},n}$ describes the interactions between the rail and the track sleeper through the rail pads. $\mathbf{K}^{\mathrm{e}}_{\mathrm{s-d},n}$ describes the interactions between the sleepers and the ballasts. $\mathbf{K}^{\mathrm{e}}_{\mathrm{r},n}$ is the stiffness matrix of the rail and has

where the subscripts TV and VT denote the interaction matrices of the vehicle-track system, which is obtained according to Eq. (17). Subscripts TS and ST represent the interaction matrices of the track and the SFT, which are connected via the subgrade system as shown in Fig. 3.

The primary parameters of a conventional SFT, as utilized in transportation infrastructure, are derived from (Jin and Kim, 2020). The SFT diameter is increased to accommodate train service. Furthermore, the longitudinal spacing of mooring lines is selected as a variable for parametric analysis. To evaluate the performance of the vehicle-track-SFT interaction under wave excitations, a representative vehicle-track model employed in high-speed railway applications (Zhai, 2020) is adopted. Table 1 summarizes the key parameters utilized in the subsequent analysis.

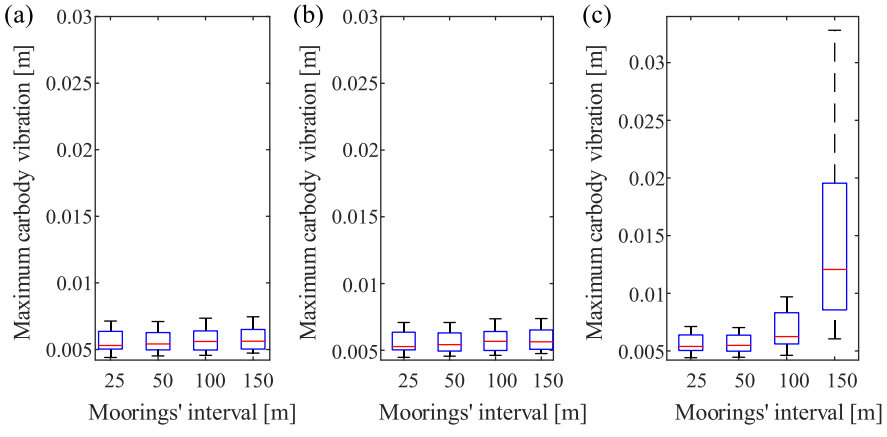

Fig. 7. Boxplot of maximum carbody displacement with different L_{m}. (a–c) Present the results with $\theta = 30°$, $\theta = 60°$ and $\theta = 90°$, respectively.

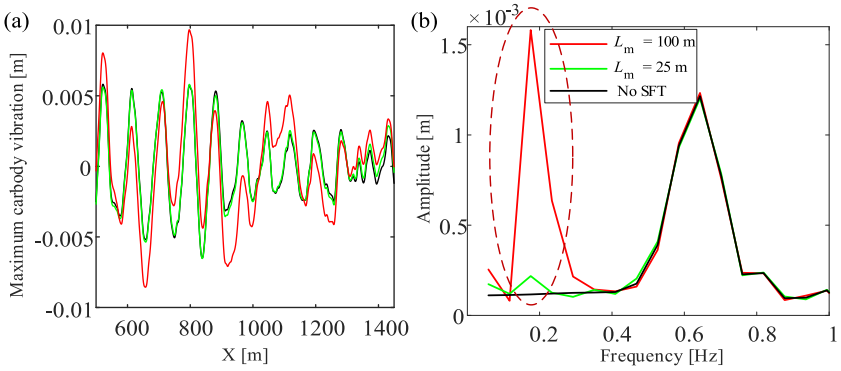

Fig. 8. Comparison of (a) time histories and (b) spectrums of carbody vibration evaluated with and without SFT ($\theta = 90°$).

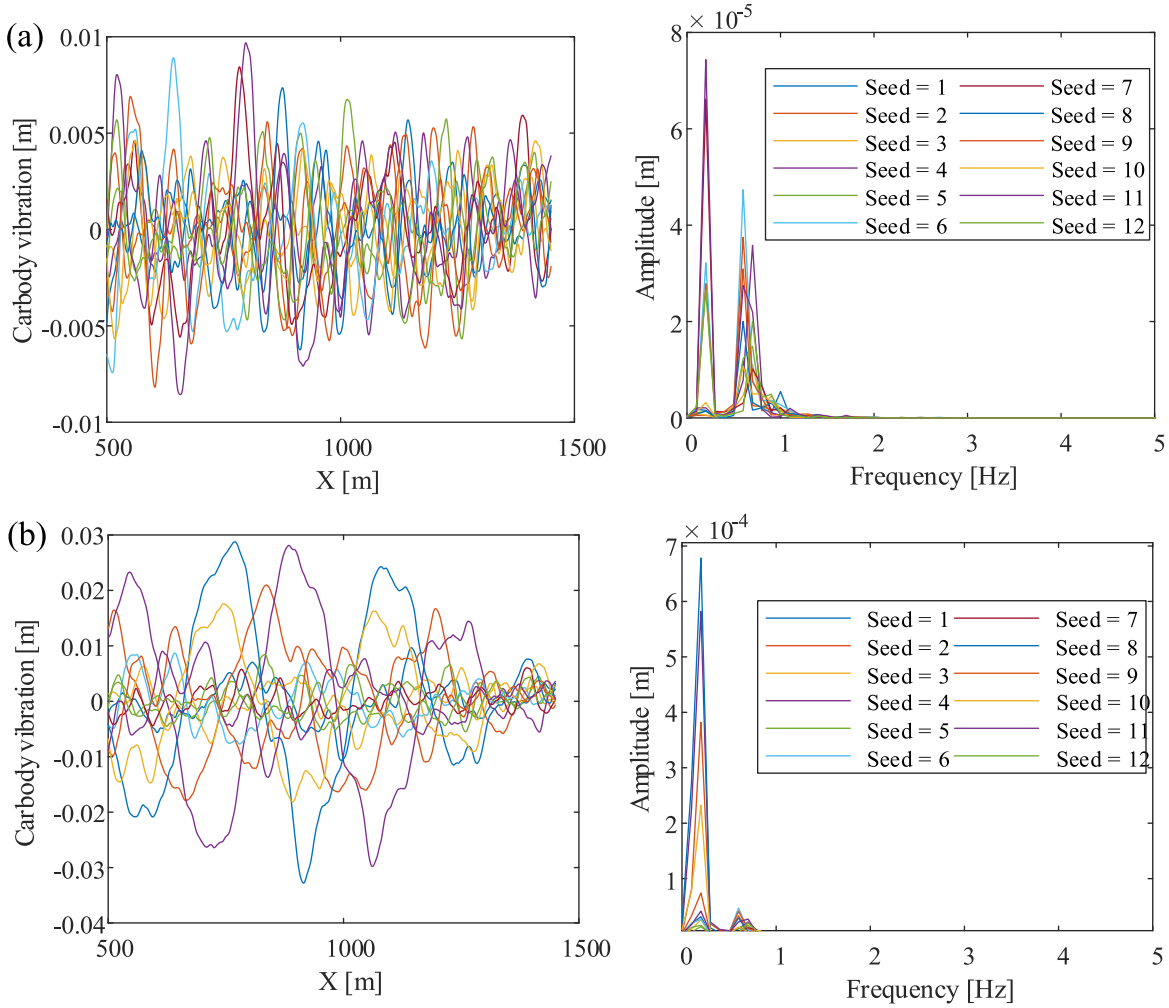

Fig. 9. Time-histories and spectrum of carbody vibration with $\theta = 90°$. (a) and (b) present the results with $L_m = 100$ m and $L_m = 150$ m, respectively.

To ensure numerical accuracy, a minuscule element length of 0.2 m is employed to discretize both the track and the SFT. The total length of the SFT-Track spans 1500 m, with a corresponding element count of 7500 for either the SFT or the Track. Each node possesses two degrees of freedom, resulting in a total of over 30,000 degrees of freedom. Within the high-speed range of 200 km/h to 320 km/h, the element passing frequency ranges from 277.78 Hz to 444.44 Hz. Notably, this frequency spectrum is several orders of magnitude higher than the frequencies relevant to the coupled system, which typically do not exceed 5 Hz. To address this, our simulation strategically employs a sampling frequency of 10,000 Hz, surpassing the magnitudes of the element passing frequencies by more than 20 times. For the assurance of convergence, we have integrated an implicit Newmark-β scheme into our simulation, complemented by a rigorous convergence condition articulated in Eq.

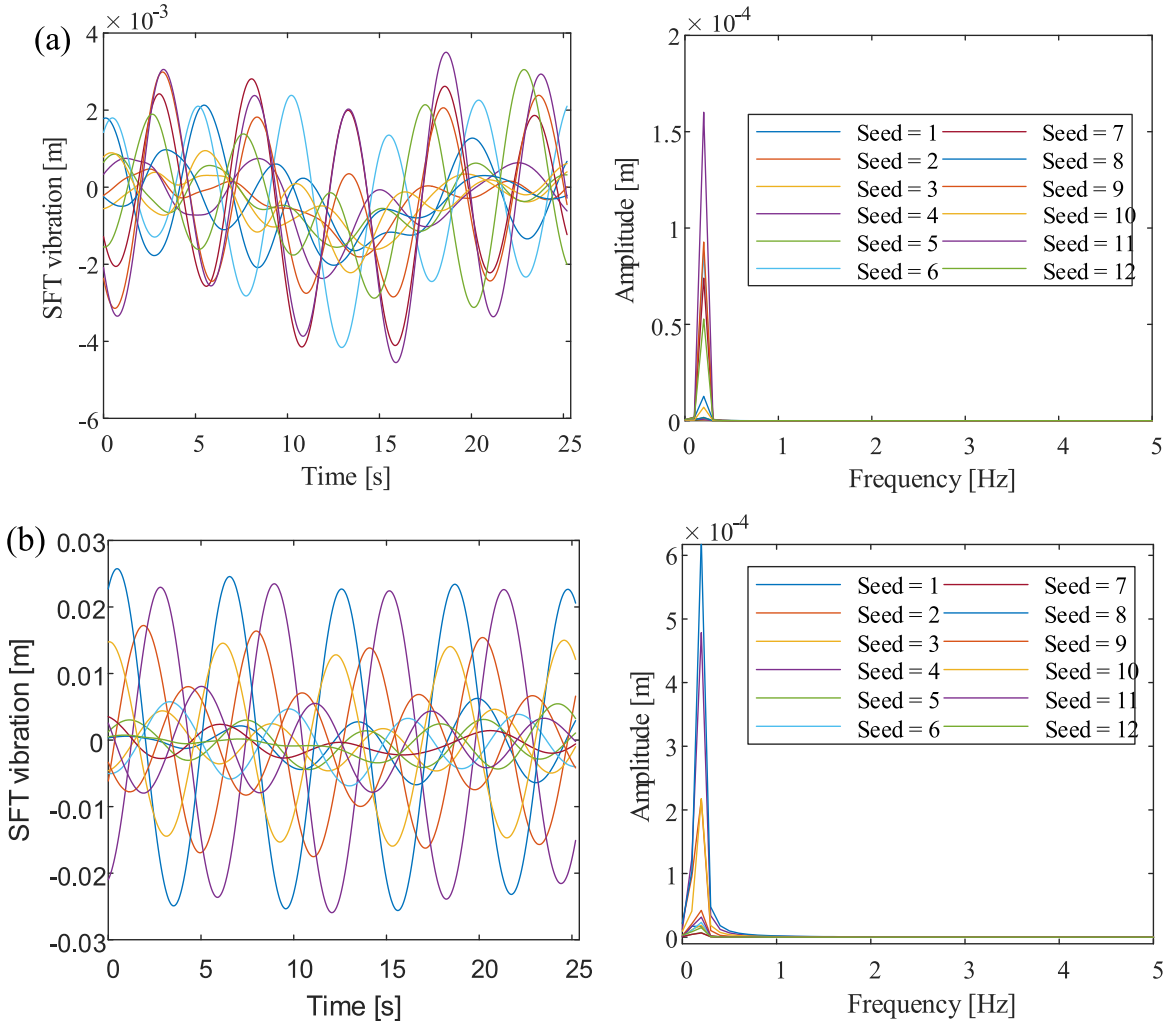

Fig. 10. Time-histories and spectrum of SFT vibration (at 800 m) with $q = 90°$. (a) and (b) present the results with $L_m = 100$ m and $L_m = 150$ m, respectively.

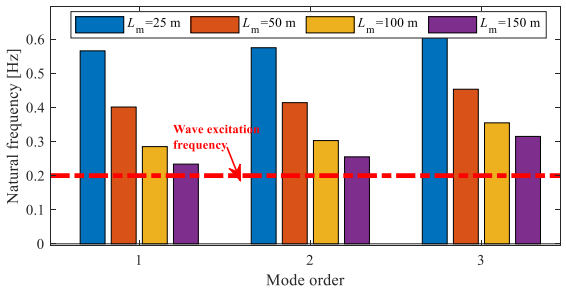

Fig. 11. Natural frequencies of the SFT-track structure with different moorings' interval.

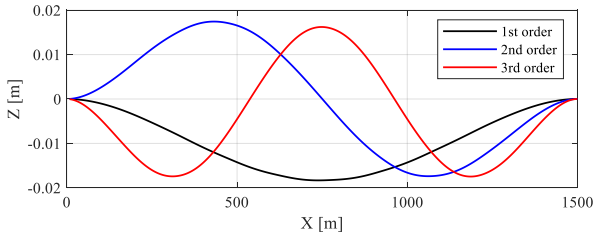

Fig. 12. Mode shape of the SFT with $L_m = 150$ m.

(20).

$$\max\left(\left|\Delta\mathbf{U}^{n+1} - \Delta\mathbf{U}^{n}\right|\right) < 10^{-10}\text{m} \tag{20}$$

Here, $\Delta\mathbf{U}$ represents the incremental displacement of the vehicle-track-SFT system, and the superscript n indicates the cycle number within each time step. The use of an exceedingly minute residual of 10^{-10} m is deliberate, ensuring a negligible error introduced by the numerical algorithm. However, it is acknowledged that this precision comes at the cost of a substantial computational burden. Initiating the simulation without the vehicle, the first 10 min focus on modelling the SFT-track system under wave excitations. This preliminary phase ensures the complete excitation of the SFT's vibration by the waves before incorporating the vehicle into the model.

3. Analysis with operational wave conditions

The operational wave condition is the predominant operating scenario for the vehicle-track-SFT system. This section focuses on conducting a series of simulations to thoroughly examine the dynamic performance of the vehicle and the SFT under the excitation of operational waves. The numerical simulations consider the following defined working conditions:

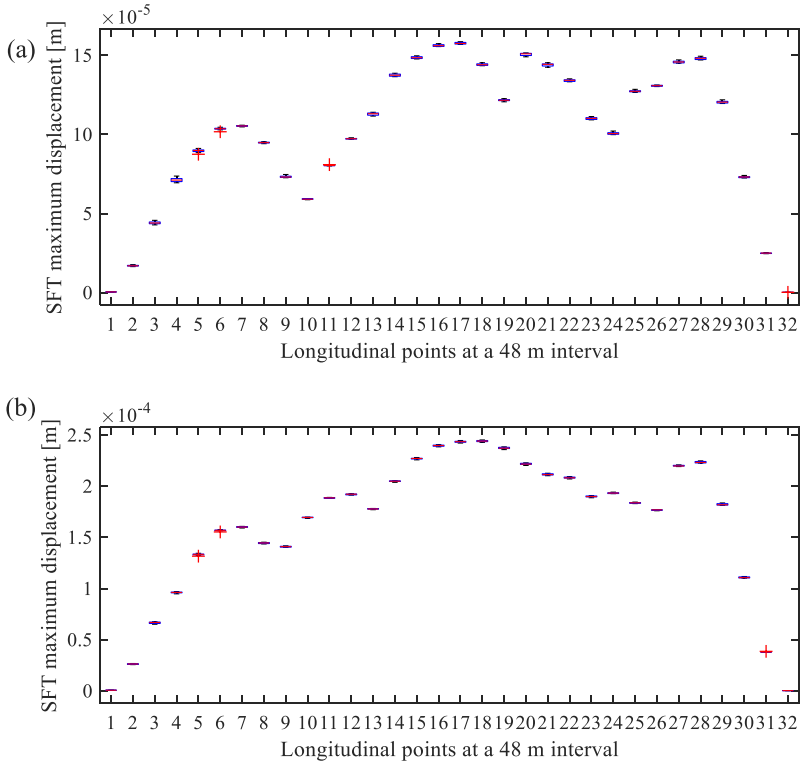

Fig. 13. Boxplots of SFT maximum displacement at different points with $\theta = 30°$. (a) and (b) present the results with $L_m = 50$ m and $L_m = 150$ m.

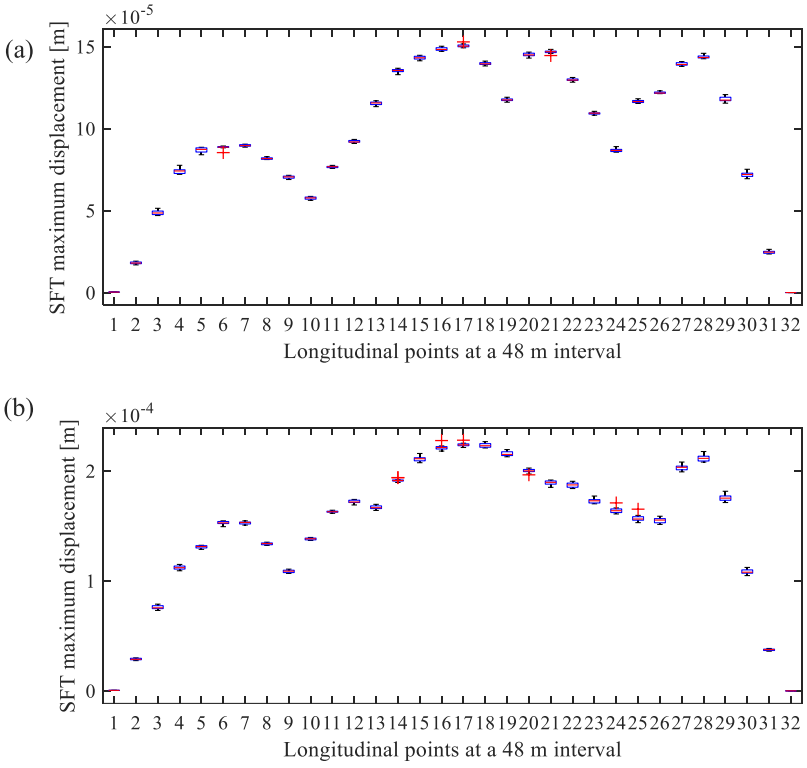

Fig. 14. Boxplot of SFT maximum displacement at different points with $\theta = 60°$. (a) and (b) present the results with $L_m = 50$ m and $L_m = 150$ m.

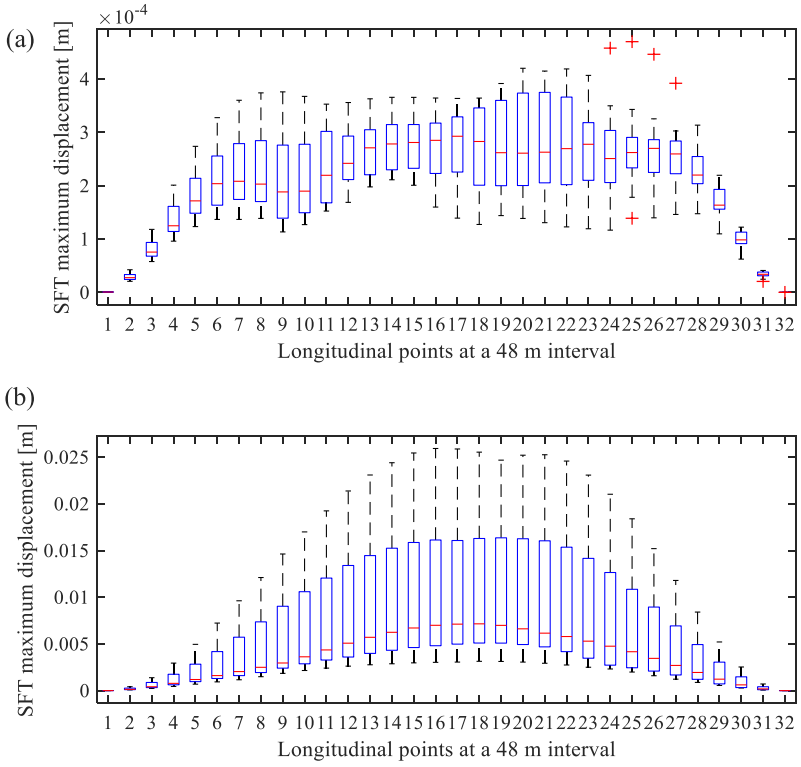

Fig. 15. Boxplot of maximum SFT displacement at different points with $\theta = 90°$. (a) and (b) present the results with $L_m = 50$ m and $L_m = 150$ m.

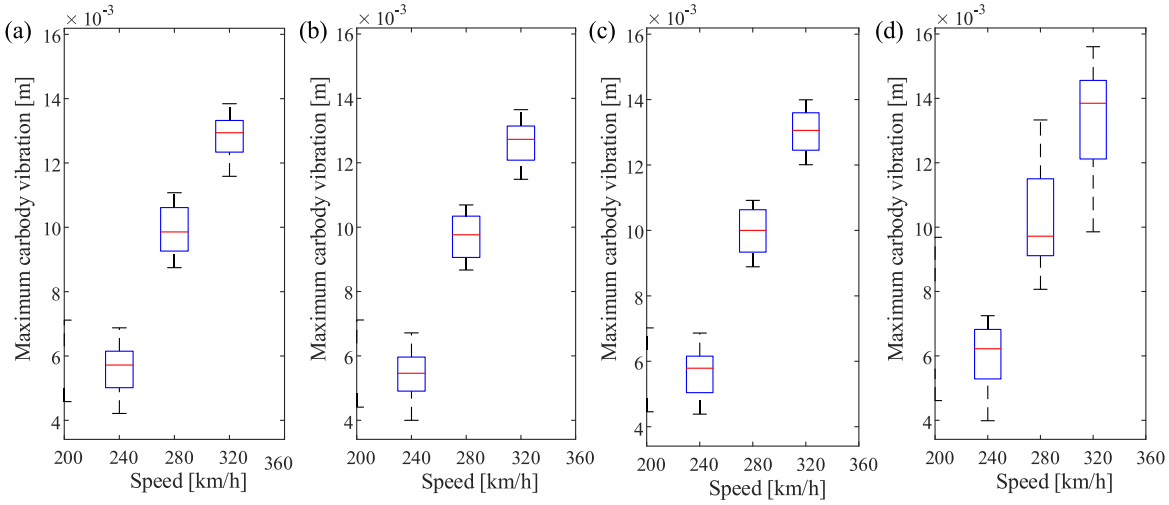

Fig. 16. Boxplot of maximum carbody displacement at different train speeds. (a) Presents the results without SFT; (b–d) present the results with $L_m = 25$ m, $L_m = 50$ m and $L_m = 100$ m, respectively.

- Wave conditions: $H_s = 3$ m; $T_p = 5$s; $\theta = 30°$, $60°$ and $90°$;
- Vehicle speed: $v = 200$ km/h, 240 km/h, 280 km/h and 320 km/h;
- Moorings' spacing: $L_m = 25$ m, 50 m, 100 m and 150 m;

From an industrial standpoint, maintaining consistent stiffness per unit is crucial when altering moorings' spacing. However, in the context of this study, our objective is to conduct a parametric analysis to investigate the impact of mooring spacing on dynamic performance within the dynamics of train operations. To effectively quantify the effect of a single parameter, it becomes necessary to hold other relevant parameters constant, thereby streamlining the analysis. The decision to keep other parameters unchanged serves the purpose of enabling a focused observation of how the interaction performance changes with variations in structural parameters. This deliberate approach enhances our ability to discern and analyse the specific influence of mooring spacing on the dynamic behaviour of the system. To quantify the dispersion in dynamic behaviour resulting from the stochastic nature of waves and track irregularities, a total of 12 simulations are conducted for each case. The primary indicators used to analyse the dynamic performance are the maximum deviation of the gravitational centre of the

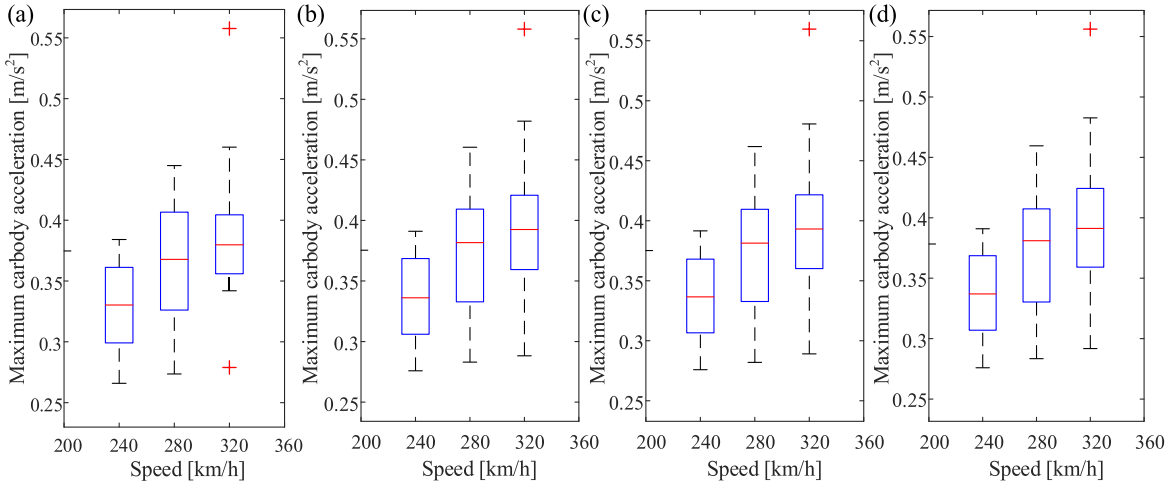

Fig. 17. Boxplot of maximum carbody acceleration with different train speeds. (a) Presents the results without SFT; (b–d) present the results with $L_m = 25$ m, $L_m = 50$ m and $L_m = 100$ m, respectively.

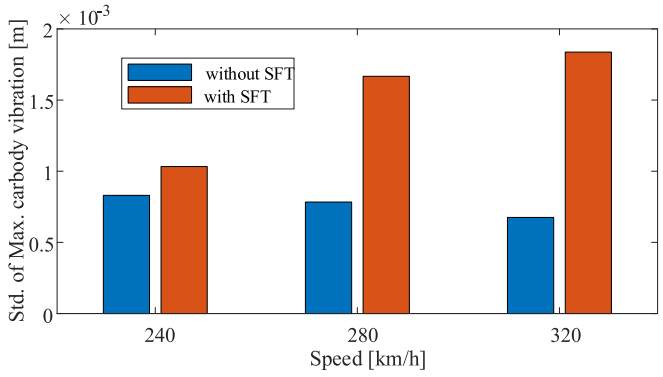

Fig. 18. Standard deviations of maximum carbody displacement at different train speeds with an SFT of Lm = 100 m and without SFT.

carbody (relative to its initial position) and the maximum acceleration. The initial position is defined at the moment when the carbody makes contact with the track-SFT. It is important to note that the utilization of 12 realizations for each case may not comprehensively capture the full spectrum of the stochastic behaviors inherent in the coupled system. However, it is crucial to clarify that the primary objective of this paper is not to rigorously pursue statistically precise quantification of the stochastic behaviors. Rather, these 12 realizations are intended to offer a meaningful evaluation of dispersion. This approach facilitates an analysis of the effects of various structural parameters on the dynamic performance, providing valuable insights without the need for an exhaustive statistical treatment. In this study, the boxplot is employed as a tool to assess the dispersion of dynamic behaviour across the simulations. The boxplot provides valuable insights into the distribution and variability of the results, enabling a comprehensive analysis of the system's performance. The boxplot is a standardized way to display the distribution of data based on a summary of five numbers, which are the minimal value Q_{min}, the first quartile Q_1, the median Q_2, the third quartile Q_3, and the maximal value Q_{max}. Usually the maximal and minimal can be calculated by the following two equations respectively.

$$Q_{max} = Q_3 + 1.5 \times IQR \tag{21a}$$

$$Q_{min} = Q_1 - 1.5 \times IQR \tag{21b}$$

in which, IQR is the range from the 25th to 75th percentile.

3.1. Analysis with the train speed of 200 km/h

At a train speed of 200 km/h, the boxplots of maximum carbody vibration are depicted in Fig. 7 for different wave headings ($\theta = 30°$, 60°, and 90°). When the wave headings are 30° and 60°, the carbody vibration remains relatively consistent, with a slight dispersion observed in each case. The maximum carbody displacement typically ranges from 0.0045 m to 0.0073 m across all cases, with a marginal increase observed with larger mooring intervals. However, when the wave heading is 90°, a significant increase in dispersion of the maximum displacement is observed at mooring intervals of 100 m and 150 m. Particularly at a mooring interval of 150 m, the dispersion range expands several magnitudes, with extreme values exceeding 0.033 m, over three times higher than other cases. Waves that are perpendicular to the SFT result in identical wave elevations acting on the entire structure at each time step, making it more susceptible to intense vibrations. Therefore, the worst-case scenario with a wave heading of 90° ($\theta = 90°$) is selected for further analysis.

To examine the difference in dynamic response between rail vehicles on land and in an SFT, Fig. 8 presents an example of time histories and spectra of carbody vibration with and without SFT. When the SFT is incorporated, two longitudinal intervals of the mooring lines as considered, namely, $L_m = 25$ m and $L_m = 100$ m. The presence of the SFT has a minimal impact on carbody vibration when L_m is 25 m. However, with L_m increased to 100 m, a significant increase in carbody vibration is observed. The spectrum reveals an additional frequency component around 0.2 Hz introduced by the presence of the SFT, which corresponds to the peak period of the wave excitation. The energy at this frequency even surpasses the natural frequency of the carbody for the case with $L_m = 100$ m.

To further investigate the cause of the pronounced surge in carbody vibration at $L_m = 150$ m, Fig. 9 (a) and (b) illustrate the time histories and spectra of carbody vibration at $L_m = 100$ m and $L_m = 150$ m, respectively, for a wave heading of 90° ($\theta = 90°$). Two significant peaks are observed in the spectrum, corresponding to the first natural frequencies of the SFT and the vehicle. The energy at the natural frequency related to the SFT experiences a sharp surge as L_m increases to 150 m, indicating intensive vibration of the SFT. Fig. 10(a) and (b) present the time histories and spectra of SFT vibration at a specific point (800 m) for $L_m = 100$ m and $L_m = 150$ m, respectively. In some cases, vibrations at $L_m = 150$ m exhibit more pronounced harmonicity, suggesting resonance triggered by the wave excitation. The spectral analysis reveals peaks at the wave excitation frequency (0.2 Hz) for both $L_m = 100$ m and $L_m = 150$ m. The observed variability in sample amplitudes for the same

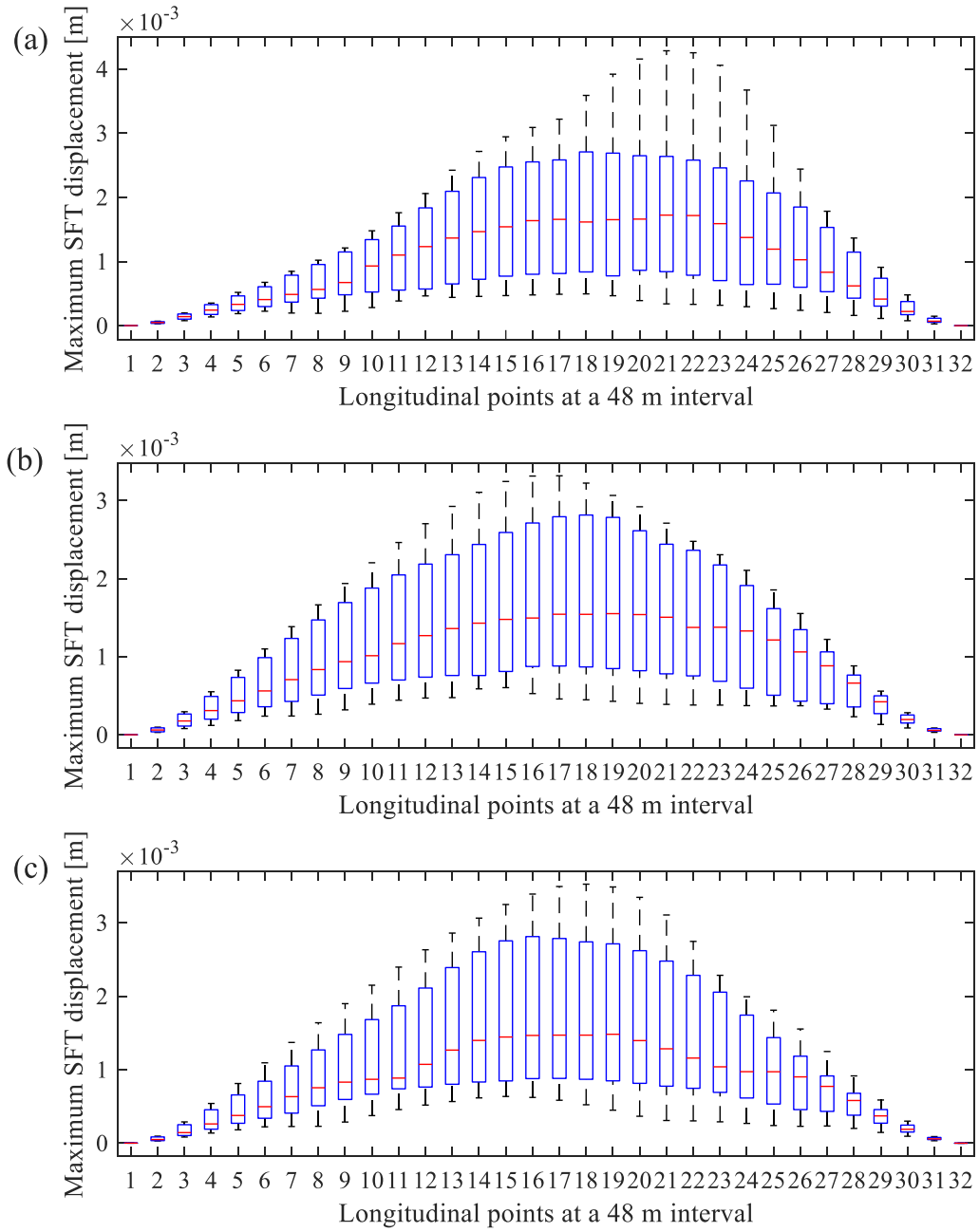

Fig. 19. Boxplot of maximum SFT displacement at different longitudinal points with $L_m = 100$ m. (a–c) Present the results with train speeds of 240 km/h, 280 km/h and 320 km/h, respectively.

case is evident in Figs. 9 and 10. These figures depict the outcomes under the most challenging conditions, considering the largest longitudinal spacing between adjacent mooring lines and a 90° wave heading, resulting in a significant amplitude disparity. A key factor contributing to this divergence is the brief duration during when the train traverses the SFT. The simulation results are confined to the time when the train passes the SFT, amplifying the influence of stochastic excitations. This is also often encountered when studying similar engineering problems such as vehicle-bridge interactions (Wang et al., 2023) and pantograph-catenary interactions (Song et al., 2023a). It underscores the necessity for conducting multiple realizations to effectively capture the dispersion of results.

Fig. 11 illustrates the natural frequencies of the SFT-track structure for different L_m values. Additionally, Fig. 12 presents the first three mode shapes of the SFT with $L_m = 150$ m. Generally, increasing L_m leads to higher natural frequencies of the SFT. At $L_m = 150$ m, the first natural frequency is 0.23 Hz, which is close to the wave excitation frequency of 0.2 Hz. This contributes to the observed resonant phenomenon at $L_m = 150$ m. Therefore, it is recommended to avoid excessive mooring intervals for the SFT to prevent potential resonance. For the analysed scenario, a mooring interval smaller than 100 m is recommended to ensure avoid resonant responses.

To analyse the vibration of the SFT under wave excitation, several observation points along the SFT are selected at a longitudinal interval of 48 m. The boxplots of maximum SFT displacement for wave headings of $\theta = 30°$, $\theta = 60°$, and $\theta = 90°$ are presented in Figs. 13–15, respectively. The analysis focuses on two scenarios: $L_m = 50$ m and $L_m = 150$ m. Generally, the dispersion of results for $\theta = 30°$ and $\theta = 60°$ is negligible. However, for $\theta = 90°$, a more significant dispersion is observed in the SFT vibration. The displacement in the middle section of

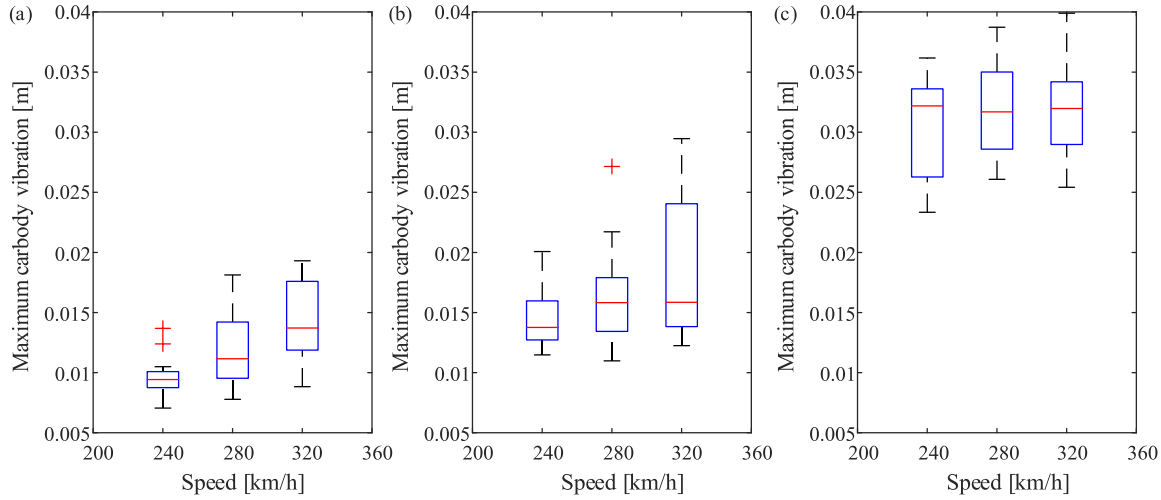

Fig. 20. Boxplot of maximum carbody vibration under rough wave conditions (a–c) present the results with $L_m = 25$ m, $L_m = 50$ m and $L_m = 100$ m, respectively.

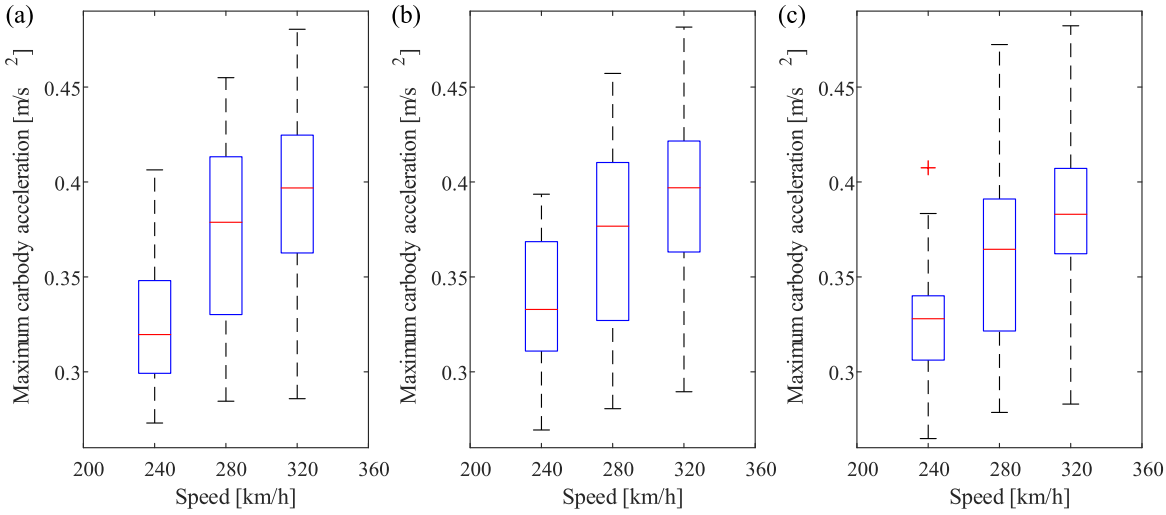

Fig. 21. Boxplot of maximum carbody acceleration under rough wave conditions (a–c) present the results with $L_m = 25$ m, $L_m = 50$ m and $L_m = 100$ m, respectively.

the SFT is greater than at the two sides and exhibits a higher dispersion. At $L_m = 150$ m, the largest displacement is over fifty times larger than the configureuration with $L_m = 50$ m, primarily due to resonant responses. In contrast, for the other two wave angles, increasing L_m from 50 m to 150 m results in a maximum displacement increase of no more than twenty times. Since the worst-case scenario with the greatest dispersion and largest displacement occurs at $\theta = 90°$, only this wave heading is considered in subsequent analyses.

3.2. Analysis with the speed upgrade

In this sub-section, the dynamic behaviour of the vehicle-track-SFT system is analysed at higher speeds. Fig. 16 presents the boxplots of maximum carbody displacement at different train speeds. Based on the previous analysis, which indicated that an excessive longitudinal spacing of the mooring lines can lead to an unacceptable level of performance, only three intervals, namely $L_m = 25$ m, 50 m, and 100 m, are considered in the simulations. Results for the land vehicle-track system without an SFT are also presented for the purpose of comparison. The corresponding results of maximum acceleration are presented in Fig. 17. It can be observed that increasing the train speed generally leads to an overall increase in maximum carbody displacement. For $L_m = 25$ m and 50 m, the dynamic behaviour of the rail vehicle within the SFT does not exhibit significant differences from conventional land rail vehicles. Thus, rail irregularity remains the dominant factor causing the dispersion of the dynamic response when the mooring lines' interval is small. However, when $L_m = 100$ m, a higher dispersion and larger vibration displacement caused by the presence of the SFT become apparent.

To quantify the increase in dispersion caused by the presence of the SFT, the standard deviations of maximum carbody displacement at different train speeds are compared between cases with an SFT of $L_m = 100$ m and without an SFT, as shown in Fig. 18. Due to the presence of the SFT, the resulting maximum carbody displacement exhibits a higher dispersion at each speed. The increase in train speed from 240 km/h to 320 km/h causes a 77.83% increase in the standard deviation of the evaluated maximum carbody displacement. However, for the traditional land rail vehicle, the increase in train speed leads to a decrease in dispersion. This provides evidence that the wave excitation is a significant factor contributing to the dispersion in the dynamic response as the train speed increases. Regarding train acceleration performances, the resulting maximum carbody acceleration also exhibits a higher dispersion with the increase in train speed. The boxplots of acceleration almost remain the same for the three different L_m values. It is important to note that the vertical carbody acceleration in high-speed railways is typically

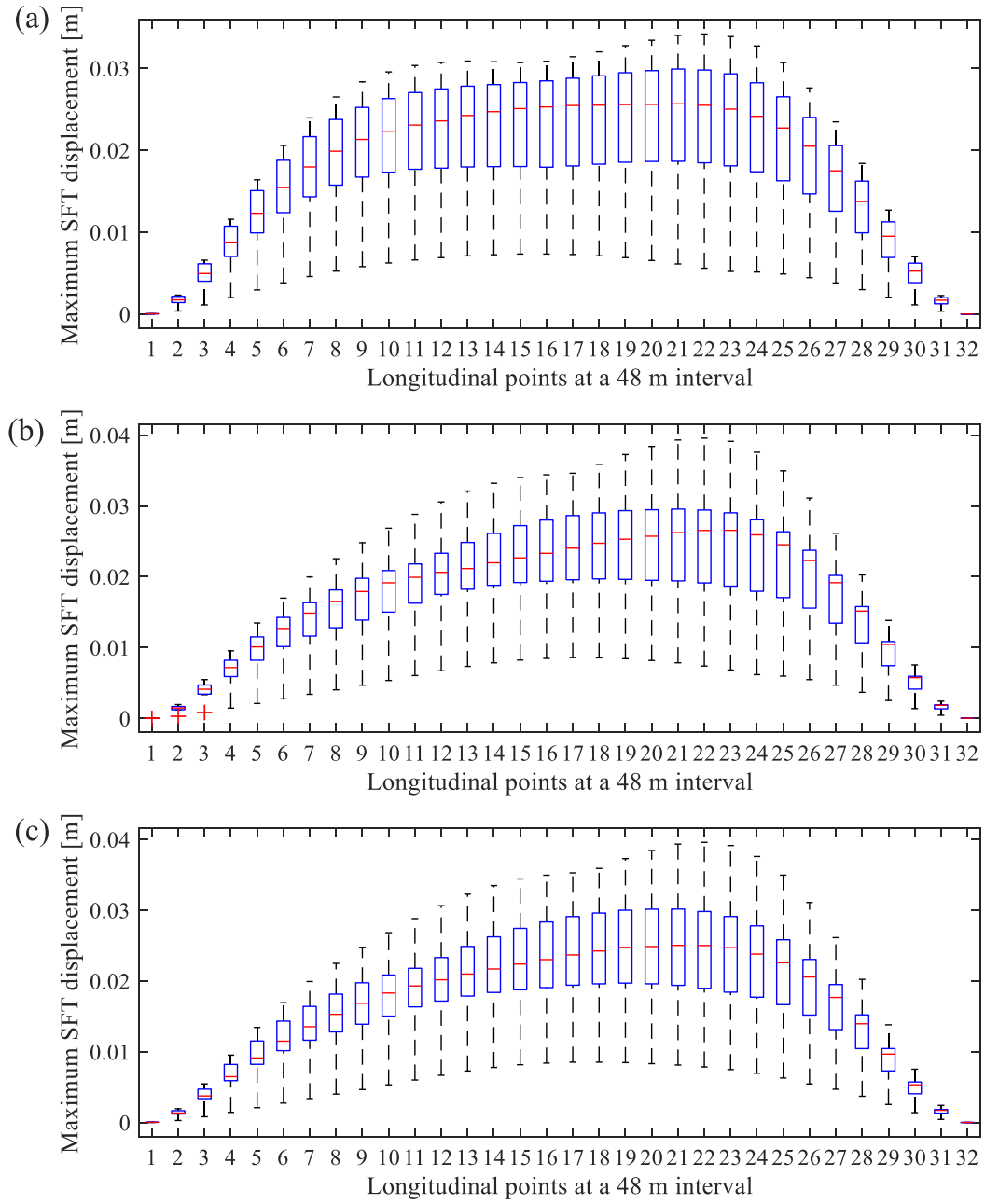

Fig. 22. Boxplot of maximum SFT displacement at different longitudinal points under rough wave conditions with $L_m = 100$ m. (a–c) Present the results with train speeds of 240 km/h, 280 km/h and 320 km/h, respectively.

limited to be lower than 0.5 m/s^2 to ensure satisfactory passenger comfort. It can be seen that passenger comfort performance is generally satisfied at these train speeds examined in this study.

To investigate the vibration of the SFT at different train speeds, Fig. 19(a)–19(c) presents the boxplots of maximum SFT displacement at various longitudinal points with $L_m = 100$ m for train speeds of 240 km/h, 280 km/h, and 320 km/h, respectively. When compared with those at 200 km/h as shown in Fig. 15, it can be observed that the SFT vibration is not significantly affected by the increase in train speed. The largest displacement of the SFT and the dispersion of the results generally remain the same for different speeds. Therefore, increasing the train speed primarily results in an increase in carbody vibration and dispersion of carbody acceleration, rather than directly affecting the vibration of the SFT.

4. Analysis with rough wave conditions

In this section, the vehicle-track-SFT dynamic performance is evaluated under rough wave conditions. According to (Suh et al., 2010), the rough wave conditions used for the subsequent analysis are defined as follows:

- Wave conditions: $H_s = 9$ m, $T_p = 7$s, $\theta = 90°$;
- Vehicle speed: $v = 200$ km/h, 240 km/h, 280 km/h and 320 km/h;
- Mooring lines' interval: $L_m = 25$ m, 50 m, 100 m.

Similar to the previous section, 12 simulations are performed for each case to account for the stochasticity of the wave excitation and track irregularity. The resulting boxplots of maximum carbody vibration with $L_m = 25$ m, $L_m = 50$ m and $L_m = 100$ m are presented in Fig. 20(a)-

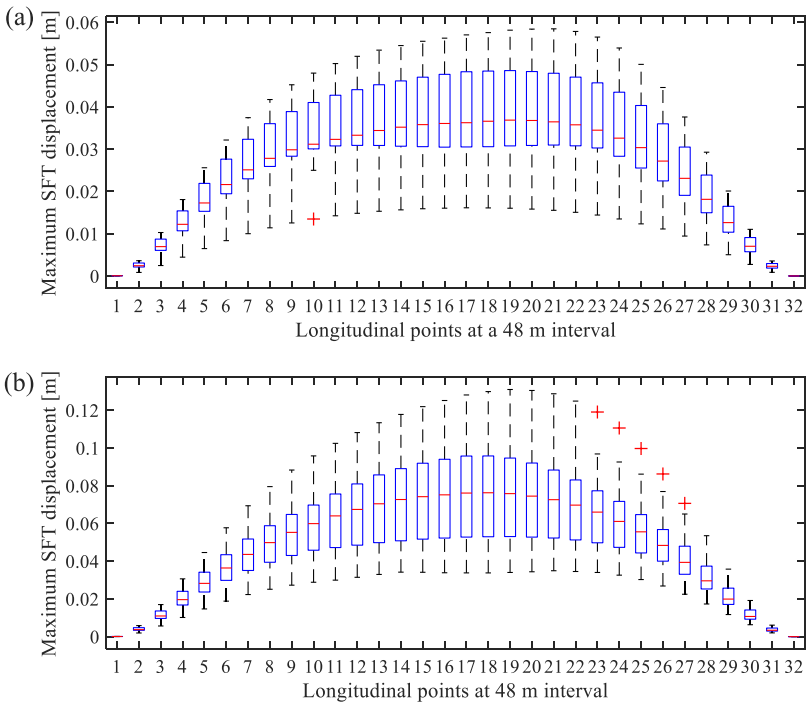

Fig. 23. Boxplot of maximum SFT displacement at different longitudinal points under rough wave conditions with $L_m = 100$ m at 320 km/h (a–b) Present the results with SFT depths of 50 m and 40 m, respectively.

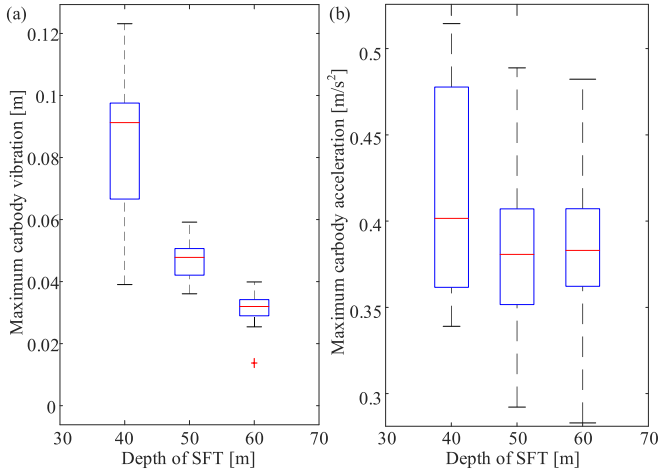

Fig. 24. Boxplot of maximum carbody displacement (a) and acceleration (b) at different longitudinal points under rough wave conditions with different installation depth of SFT.

20(c), respectively. When compared to the results under operational wave conditions in Fig. 7, it is evident that the carbody vibration exhibits a larger amplitude and higher dispersion under the excitation of rough waves. The extreme values of maximum carbody vibration with $L_m = 25$ m, $L_m = 50$ m and $L_m = 100$ m are over 10, 20 and 30 times bigger than the results under operational wave conditions, respectively. A strong sensitivity of resulting maximum carbody vibration to the mooring liness' interval can be observed. With $L_m = 100$ m, the effect of vehicle speed is not evident, which demonstrates that the wave excitation plays a dominant role in affecting the carbody vibration under rough wave conditions.

The resulting boxplots of maximum carbody acceleration with $L_m = 25$ m, $L_m = 50$ m and $L_m = 100$ m are presented in Fig. 21(a)-21(c), respectively. It is seen that the maximum carbody acceleration does not exhibit a significant change with the mooring lines' interval. The conclusions are consistent with the results under operational wave conditions, as shown in Fig. 17. This can be attributed to the significant difference in frequency between the SFT and the track. The low-frequency excitation from the SFT has a minimal impact on the carbody acceleration. Thus, it can be concluded that the carbody acceleration is not sensitive to wave excitations. Consequently, the passenger comfort performance can be generally satisfied under both the operational and rough wave conditions examined in this study.

To investigate the vibration of the SFT under rough wave conditions, Fig. 22(a)-22(c) present the boxplots of maximum SFT displacement at different longitudinal locations with $L_m = 100$ m and train speeds of 240 km/h, 280 km/h, and 320 km/h, respectively. In comparison with the results under the operational wave conditions shown in Fig. 19, it can be observed that the extreme value of maximum SFT vibration increases by over ten times under the rough wave conditions. The largest displacement of the SFT and the dispersion of the results generally remain consistent for different train speeds. Combining these results with the maximum carbody vibration results shown in Fig. 20, it is evident that the extreme value of maximum carbody vibration is generally in line with the extreme value of maximum SFT displacement. However, this consistency is not observed in Figs. 16 and 19 under operational wave conditions. This provides further evidence that the SFT vibration excited by waves is the dominant factor influencing the carbody vibration under rough wave conditions, while it only partially affects the carbody vibration under operational wave conditions.

According to Eq. (9), the SFT experiences varying wave excitations based on different installation submergence depths. Typically, the SFT cannot be installed in shallow water regions to avoid obstructing navigation and preventing disturbance from turbulent waves. The effects of installation depth on SFT and vehicle vibration are also investigated by considering another two installation depths of 40 m and 50 m in addition to the original value of 60 m considered above. In this study, a worst-case scenario is defined with $L_m = 100$ m and a train speed of 320 km/h. Fig. 23(a) and 23(b) present the boxplots of maximum SFT

displacement at different longitudinal locations with installation depths of 50 m and 40 m, respectively. Comparing these results with those in Fig. 22(c), it is evident that the maximum SFT displacement sharply increases with decreasing installation depth. Specifically, the maximum SFT displacement is nearly doubled when the installation depth decreases from 50 m to 40 m. Fig. 24(a) and (b) present the boxplots of maximum carbody displacement and acceleration, respectively. It can be observed that both the maximum carbody vibration and acceleration exhibit a significant increase with decreasing SFT installation depth. In particular, with an installation depth of 40 m, the maximum carbody acceleration in some cases exceeds the comfort threshold of 0.5 m/s^2. Therefore, a shallow installation depth for the SFT is not recommended to avoid the negative effects of large wave disturbances.

5. Conclusions

This paper presents a comprehensive investigation into the complex behaviours exhibited by the train-track-SFT system. By employing a finite element model of the track-SFT system, the study focuses on the vertical interaction between the train and track-SFT, considering random excitations from waves and track irregularities. The Monte Carlo method is utilized to capture the stochastic dynamic responses. The numerical simulations explore the influence of key SFT parameters, train speed, and wave angles on the dynamic behaviours of the carbody and SFT under two wave conditions: operational and rough. In summary, the main findings of this study are as follows:

- Waves that are perpendicular to the SFT are more likely to induce vibrations of significant magnitude. It is noteworthy that when the longitudinal spacing between moorings is sufficiently large and the natural frequency of the system aligns closely with the wave frequencies, there is a heightened risk of substantial instability and resonance.
- The dispersion of carbody displacement is greater compared to traditional land railways. Increasing the train speed primarily amplifies carbody vibration and the dispersion of carbody acceleration, while it has minimal impact on carbody acceleration or SFT vibration. Generally, passenger comfort is maintained under both operational and rough wave conditions.
- In rough wave conditions, the extreme values of maximum carbody vibration are several times larger than those in operational wave conditions. Additionally, the extreme value of maximum carbody vibration generally corresponds to the extreme value of maximum SFT displacement. Furthermore, a lower SFT installation depth significantly leads to more pronounced vibrations in the vehicle-SFT system.

Moving forward, a more precise depiction of the stochastic dispersion warrants exploration to delve deeper into the dynamic performance of the coupled system under random excitations. This future endeavor will involve extending the current two-dimensional model to a three-dimensional one, aiming specifically to assess the derailment risk associated with the passage of a train over an SFT.

CRediT authorship contribution statement

Yang Song: Writing – original draft, Visualization, Methodology, Investigation, Formal analysis, Conceptualization. **Jian Dai:** Writing – review & editing, Supervision, Methodology, Funding acquisition, Conceptualization. **Albert Lau:** Writing – review & editing, Methodology.

Declaration of competing interest

The authors declare that they have no known competing financial interests or personal relationships that could have appeared to influence the work reported in this paper.

Data availability

Data will be made available on request.

Acknowledgements

This work was supported by Konnekt, the national competence center for transportation in Norway, through the collaborative project on transport infrastructure granted to Oslo Metropolitan University (project number: 202640). Any opinions, findings, and conclusions or recommendations expressed in this paper are those of the authors and do not reflect the views of Konnekt.

References

Chakrabarti, S., Barnett, J., Kanchi, H., Mehta, A., Yim, J., 2007. Design analysis of a truss pontoon semi-submersible concept in deep water. Ocean Eng 34, 621–629. https://doi.org/10.1016/J.OCEANENG.2006.03.012.

Chen, S.Z., Feng, D.C., Sun, Z., 2021. Reliability-based vehicle weight limit determination for urban bridge network subjected to stochastic traffic flow considering vehicle-bridge coupling. Eng. Struct. 247, 113166 https://doi.org/10.1016/J.ENGSTRUCT.2021.113166.

Dai, J., Leira, B.J., Moan, T., Kvittem, M.I., 2020. Inhomogeneous wave load effects on a long, straight and side-anchored floating pontoon bridge. Mar. Struct. 72, 102763 https://doi.org/10.1016/j.marstruc.2020.102763.

Dai, J., Abrahamsen, B.C., Viuff, T., Leira, B.J., 2022. Effect of wave-current interaction on a long fjord-crossing floating pontoon bridge. Eng. Struct. 226, 114549 https://doi.org/10.1016/j.engstruct.2022.114549.

Gao, C., Xiang, Y., Yang, Y., Lin, H., 2022. Transfer matrix method for analyzing dynamic response of multi-span elastically supported SFT under moving load. Appl. Math. Model. 112, 238–261. https://doi.org/10.1016/j.apm.2022.08.004.

Guo, Q., Xu, Z., 2011. Simulation of deep-water waves based on JONSWAP spectrum and realization by MATLAB. In: Proceedings - 2011 19th International Conference on Geoinformatics. Geoinformatics 2011. https://doi.org/10.1109/GEOINFORMATICS.2011.5981100.

Jiang, B., Liang, B., Faggiano, B., Iovane, G., Mazzolani, F.M., 2018. Overview on the structural features of submerged floating tunnels. Maintenance, safety, risk, management and life-cycle performance of bridges - proceedings of the 9th international conference on bridge maintenance. Safety and Management, IABMAS 2018, 851–858. https://doi.org/10.1201/9781315189390-115/OVERVIEW-STRUCTURAL-FEATURES-SUBMERGED-FLOATING-TUNNELS-JIANG-LIANG-FAGGIANO-IOVANE-MAZZOLANI.

Jin, C., Kim, M.H., 2020. Tunnel-mooring-train coupled dynamic analysis for submerged floating tunnel under wave excitations. Appl. Ocean Res. 94, 102008 https://doi.org/10.1016/J.APOR.2019.102008.

Jin, C., Bakti, F.P., Kim, M.H., 2021. Time-domain coupled dynamic simulation for SFT-mooring-train interaction in waves and earthquakes. Mar. Struct. 75, 102883 https://doi.org/10.1016/J.MARSTRUC.2020.102883.

Kanie, S., 2010. Feasibility studies on various SFT in Japan and their technological evaluation. Procedia Eng. 4, 13–20. https://doi.org/10.1016/J.PROENG.2010.08.004.

Kunisu, H., 2010. Evaluation of wave force acting on submerged floating tunnels. Procedia Eng. 4, 99–105. https://doi.org/10.1016/J.PROENG.2010.08.012.

Kunisu, H., Mizuno, S., Mizuno, Y., Saeki, H., 1994. Study on submerged floating tunnel characteristics under the wave condition. In: Proceedings of the 4th International Offshore and Polar Engineering Conference. ISOPE 1994, Osaka, Japan, 10-15 April, 1994.

Lin, H., Xiang, Y., Yang, Y., Chen, Z., 2018. Dynamic response analysis for submerged floating tunnel due to fluid-vehicle-tunnel interaction. Ocean Eng 166, 290–301. https://doi.org/10.1016/j.oceaneng.2018.08.023.

Liu, Z., Song, Y., Gao, S., Wang, H., 2023. Review of perspectives on pantograph-catenary interaction research for high-speed railways operating at 400 km/h and above. IEEE Trans Transp Electrif. https://doi.org/10.1109/TTE.2023.3346379, 1–1.

Luo, G., Zhang, Y., Ren, Y., Guo, Z., Pan, S., 2021. Dynamic response analysis of submerged floating tunnel under impact-vehicle load action. Appl. Math. Model. 99, 346–358. https://doi.org/10.1016/J.APM.2021.06.024.

MacCamy, R.C., Fuchs, R.A., 1954. Wave Forces on Piles: A Diffraction Theory. U.S, Beach Erosion Board, p. 1954.

Martinelli, L., Barbella, G., Feriani, A., 2010. Modeling of Qiandao Lake submerged floating tunnel subject to multi-support seismic input. Procedia Eng. 4, 311–318. https://doi.org/10.1016/j.proeng.2010.08.035.

Martinelli, L., Barbella, G., Feriani, A., 2011. A numerical procedure for simulating the multi-support seismic response of submerged floating tunnels anchored by cables. Eng. Struct. 33, 2850–2860. https://doi.org/10.1016/J.ENGSTRUCT.2011.06.009.

Martire, G., Faggiano, B., Mazzolani, F.M., Zollo, A., Stabile, T.A., 2010. Seismic analysis of a SFT solution for the Messina Strait crossing. Procedia Eng. 4, 303–310. https://doi.org/10.1016/J.PROENG.2010.08.034.

Moan, T., Eidem, M.E., 2020. Floating bridges and submerged tunnels in Norway—the history and future outlook. Lecture Notes in Civil Engineering 41, 81–111. https://doi.org/10.1007/978-981-13-8743-2_5/.

Øiseth, O., Rönnquist, A., Naess, A., Sigbjörnsson, R., 2014. Estimation of extreme response of floating bridges by Monte Carlo simulation. In: Proceedings of the 9th International Conference on Structural Dynamics. EURODYN 2014, Porto, Portugal, 30 June – 2 July 2014.

Ouyang, H., 2011. Moving-load dynamic problems: a tutorial (with a brief overview). Mech. Syst. Signal Process. https://doi.org/10.1016/j.ymssp.2010.12.010.

Paik, I.Y., Oh, C.K., Kwon, J.S., Chang, S.P., 2004. Analysis of wave force induced dynamic response of submerged floating tunnel. KSCE J. Civ. Eng. 8 (5), 543–550. https://doi.org/10.1007/BF02899580.

Remseth, S., Leira, B.J., Okstad, K.M., Mathisen, K.M., Haukås, T., 1999. Dynamic response and fluid/structure interaction of submerged floating tunnels. Comput. Struct. 72, 659–685. https://doi.org/10.1016/S0045-7949(98)00329-0.

Seo, S. il, Mun, H. suk, Lee, J. ho, Kim, J. ha, 2015. Simplified analysis for estimation of the behavior of a submerged floating tunnel in waves and experimental verification. Mar. Struct. 44, 142–158. https://doi.org/10.1016/J.MARSTRUC.2015.09.002.

Shao, Y.-L., You, J., Glomnes, E.B., 2016. Stochastic linearization and its application in motion analysis of cylindrical floating structure with bilge boxes. In: Proceedings of the 35th International Conference on Ocean, Offshore and Arctic Engineering. Busan, South Korea. https://doi.org/10.1115/OMAE2016-55059, 19-24 June, 2016. OMAE2016-55059.

Song, Y., Liu, Zhigang, Ronnquist, A., Navik, P., Liu, Zhendong, 2020. Contact wire irregularity stochastics and effect on high-speed railway pantograph-catenary interactions. IEEE Trans. Instrum. Meas. 69, 8196–8206. https://doi.org/10.1109/TIM.2020.2987457.

Song, Y., Wang, Z., Liu, Z., Wang, R., 2021. A spatial coupling model to study dynamic performance of pantograph-catenary with vehicle-track excitation. Mech. Syst. Signal Process. 151, 107336 https://doi.org/10.1016/j.ymssp.2020.107336.

Song, Y., Mei, G., Liu, Z., Gao, S., 2023a. Assessment of railway pantograph-catenary interaction performance with realistic pantograph strip imperfection. Veh. Syst. Dyn. 1–20. https://doi.org/10.1080/00423114.2023.2289662.

Song, Y., Rønnquist, A., Jiang, T., Nåvik, P., 2023b. Railway pantograph-catenary interaction performance in an overlap section: modelling, validation and analysis. J. Sound Vib. 548, 117506 https://doi.org/10.1016/J.JSV.2022.117506.

Suh, K.D., Kwon, H.D., Lee, D.Y., 2010. Some statistical characteristics of large deepwater waves around the Korean Peninsula. Coast Eng 57, 375–384. https://doi.org/10.1016/J.COASTALENG.2009.10.016.

Tariverdilo, S., Mirzapour, J., Shahmardani, M., Shabani, R., Gheyretmand, C., 2011. Vibration of submerged floating tunnels due to moving loads. Appl. Math. Model. 35, 5413–5425. https://doi.org/10.1016/J.APM.2011.04.038.

Wang, Z., Song, Y., Yin, Z., Wang, R., Zhang, W., 2019. Random response analysis of axle-box bearing of a high-speed train excited by crosswinds and track irregularities. IEEE Trans. Veh. Technol. 68, 10607–10617. https://doi.org/10.1109/TVT.2019.2943376.

Wang, L., Zhang, X., Bu, X., Han, Y., Zhu, Z., Cai, C., 2023. PDEM-based stochastic analysis of a train-track-bridge system using dimension-reduced simulations of turbulent winds and track irregularities. Struct Infrastruct Eng 19, 1795–1810. https://doi.org/10.1080/15732479.2022.2058560.

Wu, Z., Wang, D., Ke, W., Qin, Y., Lu, F., Jiang, M., 2021. Experimental investigation for the dynamic behavior of submerged floating tunnel subjected to the combined action of earthquake, wave and current. Ocean Eng 239, 109911. https://doi.org/10.1016/J.OCEANENG.2021.109911.

Xiang, Y., Yang, Y., 2016. Challenge in design and construction of submerged floating tunnel and state-of-art. Procedia Eng. 166, 53–60. https://doi.org/10.1016/J.PROENG.2016.11.562.

Xiang, Y., Lin, H., Bai, B., Chen, Z., Yang, Y., 2021. Numerical simulation and experimental study of submerged floating tunnel subjected to moving vehicle load. Ocean Eng 235, 109431. https://doi.org/10.1016/J.OCEANENG.2021.109431.

Yang, Y., Xiang, Y., Lin, H., Chen, Z., 2021. Study on vibration response of submerged floating tunnel considering vehicle eccentric load. Appl. Ocean Res. 110 https://doi.org/10.1016/j.apor.2021.102598.

Yang, Y., Xiang, Y., Gao, C., 2022a. Vehicle-SFT-current coupling vibration of multi-span submerged floating tunnel, part I: mode superposition and Galerkin hybrid method. Ocean Eng 247. https://doi.org/10.1016/j.oceaneng.2022.110746.

Yang, Y., Xiang, Y., Gao, C., 2022b. Vehicle-SFT-current coupling vibration of multi-span submerged floating tunnel, Part II: comparative analysis of finite difference method and parametric study. Ocean Eng 249, 110951. https://doi.org/10.1016/J.OCEANENG.2022.110951.

Zhai, W., 2020, fourth ed.. Vehicle–Track Coupled Dynamics Models. Vehicle–Track Coupled Dynamics. Science Press, Beijing. https://doi.org/10.1007/978-981-32-9283-3_2.

Zhai, W., Han, Z., Chen, Z., Ling, L., Zhu, S., 2019. Train–track–bridge dynamic interaction: a state-of-the-art review. Veh. Syst. Dyn. 57, 984–1027. https://doi.org/10.1080/00423114.2019.1605085.

Zhang, Y., Yang, X., 2016. Online ordering policies for a two-product, multi-period stationary newsvendor problem. Comput. Oper. Res. 74, 143–151. https://doi.org/10.1016/J.COR.2016.04.031.

Zhang, W., Zeng, J., li, Y., 2013. A review of vehicle system dynamics in the development of high-speed trains in China. Int J Dyn Control 1, 81–97. https://doi.org/10.1007/S40435-013-0005-1/FIGURES/23.

Zhang, H., Yang, Z., Li, J., Yuan, C., Xie, M., Yang, H., Yin, H., 2021. A global review for the hydrodynamic response investigation method of submerged floating tunnels. Ocean Eng 225, 108825. https://doi.org/10.1016/J.OCEANENG.2021.108825.